

Efficient Training of Boltzmann Generators Using Off-Policy Log-Dispersion Regularization

Henrik Schopmans^{1,2} Christopher von Klitzing¹ Pascal Friederich^{1,2}

Abstract

Sampling from unnormalized probability densities is a central challenge in computational science. Boltzmann generators are generative models that enable independent sampling from the Boltzmann distribution of physical systems at a given temperature. However, their practical success depends on data-efficient training, as both simulation data and target energy evaluations are costly. To this end, we propose **off-policy log-dispersion regularization (LDR)**, a novel regularization framework that builds on a generalization of the log-variance objective. We apply LDR in the off-policy setting in combination with standard data-based training objectives, without requiring additional on-policy samples. LDR acts as a shape regularizer of the energy landscape by leveraging additional information in the form of target energy labels. The proposed regularization framework is broadly applicable, supporting unbiased or biased simulation datasets as well as purely variational training without access to target samples. Across all benchmarks, LDR improves both final performance and data efficiency, with sample efficiency gains of up to one order of magnitude.

1. Introduction

Sampling from complex, high-dimensional probability distributions is a central problem in computational physics, biology, and related areas. One such task is sampling from the Boltzmann distribution of physical systems, where $\tilde{p}_X(x) = \exp\left(\frac{-E(x)}{k_B T}\right)$ is an unnormalized density, $x \in X$ is the configuration (e.g., particle positions in \mathbb{R}^{3N}), E an

¹Institute for Anthropomatics and Robotics, Karlsruhe Institute of Technology, Kaiserstr. 12, 76131 Karlsruhe, Germany ²Institute of Nanotechnology, Karlsruhe Institute of Technology, Kaiserstr. 12, 76131 Karlsruhe, Germany. Correspondence to: Pascal Friederich <pascal.friederich@kit.edu>.

energy function, T the temperature, and k_B the Boltzmann constant. The normalized distribution is $p_X(x) = \tilde{p}_X(x)/\mathcal{Z}$ with $\mathcal{Z} = \int_{X_0} \tilde{p}_X(x) dx$, where the integral is taken over X_0 corresponding to configurations with vanishing center of mass. The normalization constant \mathcal{Z} is usually unknown and intractable.

Sampling from the Boltzmann distribution enables exploring typical configurations and estimating physically relevant expectations, e.g., in drug discovery where protein-ligand binding free energies require extensive exploration of thermodynamic ensembles (Hollingsworth & Dror, 2018). Classical sampling techniques, such as molecular dynamics (MD) (Alder & Wainwright, 1959) and Markov chain Monte Carlo (MCMC) (Metropolis et al., 1953), are asymptotically correct but typically rely on long, correlated trajectories. As dimensionality and energetic complexity increase, these methods can become prohibitively expensive, particularly when energy evaluations are costly.

Generative modeling offers a complementary perspective by framing sampling as a one-shot generation problem. Boltzmann generators (Noé et al., 2019) enable independent sampling from equilibrium distributions at a given temperature, making them an attractive alternative or complement to trajectory-based methods. However, realizing a practical advantage crucially depends on data-efficient training procedures. Standard training objectives to train Boltzmann generators typically rely on equilibrium samples from the target distribution (Tan et al., 2025b; Klein & Noé, 2024) or require extensive energy evaluations in the variational setting (Schopmans & Friederich, 2025; von Klitzing et al., 2025), both of which may be limiting in realistic settings.

To address these limitations, we introduce **off-policy log-dispersion regularization (LDR)**, a general regularization framework for training Boltzmann generators more efficiently. LDR builds on a generalization of the log-variance objective, which has previously been used as a divergence for on-policy¹ variational training (Richter & Berner, 2023). In contrast, we apply LDR off-policy on fixed datasets as a regularizer on top of standard data-based objectives. LDR uses target energy labels to regularize the shape of the

¹Using samples from the model distribution for training.

learned energy landscape. Importantly, LDR can be evaluated over arbitrary reference distributions and can therefore leverage biased simulation data or auxiliary energy-labeled datasets that are otherwise difficult to incorporate.

The proposed framework applies to training on unbiased equilibrium data, biased simulation data, and even purely variational training without access to target samples. Across diverse benchmarks, we show that LDR significantly improves final model performance and data efficiency.

We summarize our contribution as follows:

- We propose log-dispersion objectives as a generalization of the log-variance objective and use them as an off-policy regularizer on top of standard data-based objectives.
- We show that log-dispersion regularization significantly increases final performance and data efficiency, both when training on unbiased and biased datasets.
- We show that log-dispersion regularization can also be adapted for variational training without target samples, improving the efficiency of the current state-of-the-art method, Constrained Mass Transport (CMT) (von Klitzing et al., 2025), by up to a factor of 10.

2. Related Work

Boltzmann generators were first introduced as an approach to obtain independent samples from Boltzmann distributions by learning an invertible generative model that supports exact likelihoods and importance reweighting (Noé et al., 2019). Closely related, Boltzmann emulators focus on learning data-driven models of approximate equilibrium ensembles, without exact reweighting guarantees (Jing et al., 2024; Lewis et al., 2024; Zheng et al., 2024).

Since their introduction, many works have studied Boltzmann generators trained from simulation data using standard data-based objectives, including discrete normalizing flows (Midgley et al., 2023; Tan et al., 2025a; Rehman et al., 2025c;b), flow matching approaches (Klein et al., 2023; Rehman et al., 2025a), and diffusion-based Boltzmann generators (Zhang et al., 2025). Several works investigate transferability, training on some molecular systems and transferring to unseen ones to amortize simulation cost (Jing et al., 2022; Abdin & Kim, 2024; Klein & Noé, 2024; Tan et al., 2025b).

Beyond data-based training, Boltzmann generators can also be learned variationally using only target energy evaluations, without access to target samples. Variational methods based on discrete normalizing flows have advanced substantially in this regime (Stimper et al., 2022; Midgley et al., 2022;

Schopmans & Friederich, 2025; von Klitzing et al., 2025), with recent approaches currently representing strong performance for variational training in molecular systems (von Klitzing et al., 2025). Diffusion-based variational counterparts have also emerged (Liu et al., 2025; Choi et al., 2025; Kim et al., 2025), but have so far been less competitive on molecular benchmarks; notably, variational diffusion training on alanine dipeptide was only recently demonstrated (Liu et al., 2025), whereas flow-based approaches reached this earlier and have since scaled to larger systems (Midgley et al., 2022; von Klitzing et al., 2025).

Finally, several recent works explore training on data at elevated temperatures and annealing toward lower temperatures, combining generative modeling with tempering or progressive annealing schedules (Dibak et al., 2022; Wahl et al., 2025; Schopmans & Friederich, 2025; Rissanen et al., 2025; Akhoud-Sadegh et al., 2025).

A key limitation across related work is data efficiency: in data-based approaches, the training signal typically comes from matching the sample distribution and does not directly leverage target energy values typically available through dataset generation. Likewise, in variational training, current state-of-the-art methods optimize objectives that do not include a direct training signal from target energy labels (Schopmans & Friederich, 2025; von Klitzing et al., 2025). Motivated by this gap, we introduce LDR, which improves data efficiency across a broad range of training settings. Similarly to our work, Vaitl et al. (2023); Vaitl & Klein (2025) recently made an important step by improving the forward KL with a path-gradient formulation, yielding a lower-variance learning signal that incorporates gradients of the target density. Compared to this approach, LDR (i) is a general off-policy regularization framework that can be evaluated on arbitrary reference distributions (including biased or auxiliary energy-labeled datasets), and (ii) directly leverages target energies rather than target gradients. Finally, LDR is complementary to path gradients and can be used on top of the path-gradient forward KL as an additional energy-based regularizer.

3. Method

To fit Boltzmann generators to a data distribution, they are typically trained with data-based objectives that do not use target energy values, even though these are usually available when constructing the dataset. Discrete normalizing flows are commonly trained via the forward KL divergence, continuous normalizing flows via flow matching, and diffusion models via score matching. While effective, these objectives rely solely on samples and ignore structure provided by the target energy landscape.

A way to incorporate target energy information is to directly

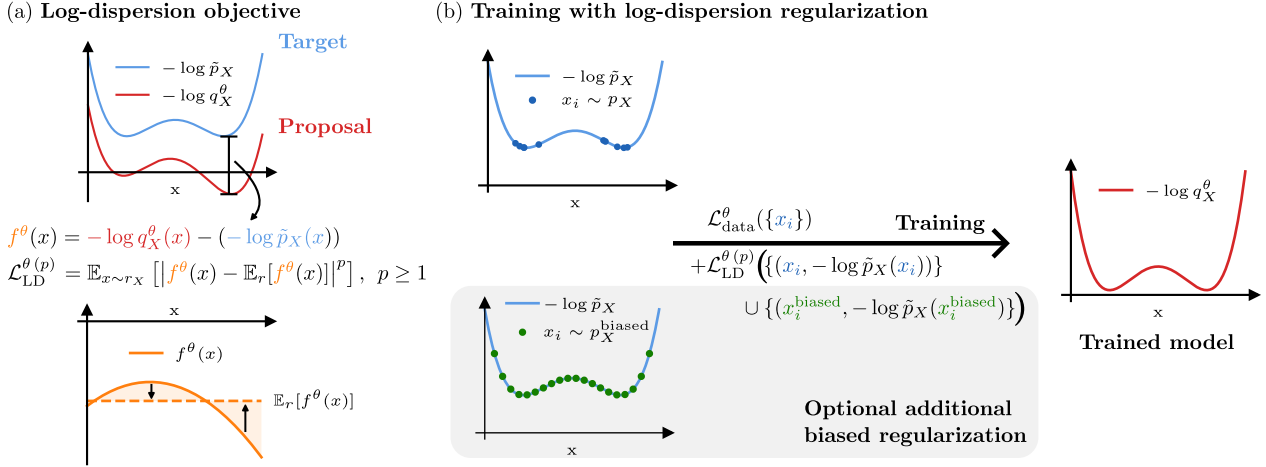


Figure 1. (a) The log-dispersion objective minimizes the dispersion of $f^\theta(x) = -\log q_X^\theta(x) - (-\log \tilde{p}_X(x))$ around its mean, regularizing the shape of the proposal q_X^θ over the support of a reference distribution r_X . (b) When training off-policy, e.g., with a fixed dataset, log-dispersion alone is not a divergence because it does not constrain the proposal outside the support of r_X . We therefore use log-dispersion as a shape regularizer on top of data-based divergences to ensure global normalization. Since the reference distribution r_X is flexible, LDR can be applied to target samples $x_i \sim p_X$ as well as biased samples $x_i^{biased} \sim p_X^{biased}$.

compare the model log-density $\log q_X^\theta(x)$ to the unnormalized target log density $\log \tilde{p}_X(x)$. We define $f^\theta(x)$ as the difference of the negative log densities (unnormalized log importance weights)

$$f^\theta(x) = -\log q_X^\theta(x) - (-\log \tilde{p}_X(x)) \quad (1)$$

$$= -\log q_X^\theta(x) - \frac{E(x)}{k_B T}. \quad (2)$$

At the optimum we have $q_X^\theta = p_X$, and thus $f^\theta(x) = \log \mathcal{Z} = \text{const.}$ (see Figure 1a for an illustration). To obtain this optimum, the log-variance objective (Richter et al., 2020) minimizes the variance of $f^\theta(x)$ under a reference distribution $r_X(x)$:

$$\mathcal{L}_{LV}^\theta = \mathbb{E}_{r_X} [(f^\theta(x) - \mathbb{E}_{r_X}[f^\theta(x)])^2]. \quad (3)$$

If $r_X(x)$ has full support, this objective defines a divergence whose minimum is achieved if and only if $q_X^\theta = p_X$, assuming that q_X^θ is properly normalized. In practice, full support is often obtained (ignoring finite-sample effects) by choosing $r_X(x) = q_X^\theta(x)$, which yields an on-policy variational objective, but requires repeated target energy evaluations and is prone to mode collapse in the finite-sample regime. On the other hand, using a fixed off-policy distribution as $r_X(x)$ lacks full support, leaving the model unconstrained and arbitrarily normalized outside the data manifold.

We generalize the log-variance objective to a family of log-dispersion objectives that minimize the dispersion of $f^\theta(x)$ around its mean,

$$\mathcal{L}_{LD}^{\theta(p)} = \mathbb{E}_{r_X} [|f^\theta(x) - \mathbb{E}_{r_X}[f^\theta(x)]|^p], \quad p \geq 1. \quad (4)$$

While the log-variance objective corresponds to $p = 2$ and minimizes the second central moment (variance), we additionally consider the L1 log-dispersion objective ($p = 1$), which minimizes the first absolute central moment. We hypothesize that this objective is less sensitive to outliers and numerically more stable, an important property for Boltzmann generators, where energy values can span multiple orders of magnitude. Some related diffusion sampling works replace the mean in Equation 4 with a learnable scalar parameter (trajectory balance objective) (Sendera et al., 2024). Here, we simply use the batch-wise mean and backpropagate through both $f^\theta(x)$ and $\mathbb{E}_{r_X}[f^\theta(x)]$.

Rather than using log-dispersion objectives on-policy as a standalone variational divergence, we propose to combine them with a standard data-based objective,

$$\mathcal{L}^\theta = \lambda_{data} \mathcal{L}_{data}^\theta + \lambda_{LD} \mathcal{L}_{LD}^{\theta(p)}. \quad (5)$$

Figure 1b illustrates the training procedure using this log-dispersion regularization. The data-based term ensures correct normalization and convergence to the target distribution

over the full space, while the log-dispersion term acts as a shape regularizer that aligns the proposal with the target energy landscape by minimizing dispersion in the log importance weights. This hybrid formulation provides an additional training signal through the incorporation of target energy labels. Importantly, LDR can be evaluated over arbitrary reference distributions and is not restricted to the target distribution itself. Furthermore, in contrast to on-policy training with log-dispersion objectives, our approach solely relies on a fixed dataset with target energy labels, as it is usually already available after performing unbiased or biased MD simulations. It does not use additional target energy evaluations during training.

4. Experiments

4.1. Experimental Setup

Architecture One key property of Boltzmann generators is the ability to asymptotically unbias the generated distribution using importance weights $w(x) = \frac{\tilde{p}_X(x)}{q_X^\theta(x)}$. For some observable $h(x)$ it holds (Martino et al., 2017; Noé et al., 2019)

$$\sum_{n=1}^N \frac{w(x_n)}{\sum_{i=1}^N w(x_i)} h(x_n) \xrightarrow{N \rightarrow \infty} \int h(x) p_X(x) dx. \quad (6)$$

While generative approaches such as continuous normalizing flows and diffusion models have shown strong performance, correcting their sampling bias via importance sampling is typically computationally expensive (Tan et al., 2025a; Klein & Noé, 2024). Recent works focused on cheaper unbiasing of continuous normalizing flows or diffusion models (Zhang et al., 2025; Peng & Gao, 2025), though no general solution is currently available. In contrast, discrete normalizing flows provide exact and inexpensive likelihood evaluations by construction. This property is especially critical in the context of Boltzmann generators, where unbiased estimates of thermodynamic quantities are required. For these reasons, we adopt discrete normalizing flows as the generative backbone in this work.

For individual molecular systems, normalizing flows defined on internal coordinate representations currently achieve state-of-the-art performance in both data-based and variational training regimes (Kim et al., 2024; von Klitzing et al., 2025). However, the choice of coordinate representation involves an inherent tradeoff: internal coordinates are system-specific and non-unique, which limits their transferability across different molecules. In contrast, Boltzmann generators operating directly on Cartesian coordinates offer a more flexible and transferable framework, but their performance still falls short of what can be achieved using internal

coordinate representations (Klein & Noé, 2024; Tan et al., 2025b).

We use a two-step experimental setup. First, we evaluate LDR using normalizing flows in an internal coordinate representation, which are substantially cheaper to train and evaluate and yield stronger final performance. We focus on controlled single-system benchmarks rather than transferability, where the non-uniqueness of internal coordinates would be a limiting factor. Second, to show that LDR is not tied to a particular coordinate choice, we report experiments in Cartesian coordinates in Section 4.5. For architecture details, see Appendix B.1.

Target densities To benchmark LDR, we first use the well-studied alanine dipeptide ($d = 60$) (Dibak et al., 2022; Stimper et al., 2022; Midgley et al., 2022; Tan et al., 2025b) system, a common benchmark in prior work. We further use the larger alanine hexapeptide ($d = 180$) (Schopmans & Friederich, 2025; von Klitzing et al., 2025) to test the scalability of our method. Both systems have complex metastable regions that occupy only a small part of the overall state space, making them well-suited as challenging benchmarks.

Metrics As metrics, we first use the negative log-likelihood defined as $\text{NLL} = -\mathbb{E}_{x \sim p_X(x)} [\log q_X^\theta(x)]$. The NLL is equivalent to the forward KL divergence up to an additive constant, and thus provides a reliable signal for mode collapse (Blessing et al., 2024) and model performance.

We additionally report the effective sample size (ESS), which quantifies how many independent draws from the target distribution p_X would be required to attain the same estimator variance as that obtained using samples from the flow distribution q_X^θ (Martino et al., 2017). In practice, we compute the reverse ESS from flow samples (Martino et al., 2017). Since the reverse ESS is restricted to the support of q_X^θ , a large ESS can occur under mode collapse; we therefore always assess it jointly with NLL.

We introduce and report additional metrics in Appendix B.5. In the main manuscript, consistent with recent work (Klein & Noé, 2024; Vaitl & Klein, 2025), we focus on NLL and ESS, which we found most reliable for assessing relative performance. However, NLL is not normalized, and its absolute scale is not directly interpretable, so even small differences can be significant. We therefore use NLL primarily to rank methods and refer to the metrics in the appendix when additional nuance is required.

We further refer to Figure 7 in Appendix F for a visualization of the 2D marginal densities of the main degrees of freedom of each system (Ramachandran plots and TICA plots).

Table 1. Results for training on unbiased datasets from the target distribution. We report negative log-likelihood (NLL; lower is better) and effective sample size (ESS; higher is better), averaged over 4 independent experiments with standard deviations. For each number of samples, **bold** indicates methods whose performance is not statistically significantly different from the best-performing method (two-sided Welch’s t-test with $p \geq 0.05$). Right: ESS as a function of the number of training samples.

SYSTEM	# SAMPLES	METHOD	NLL \downarrow	ESS / % \uparrow	FWD KL FWD KL (path) FWD KL + LDR-L2 (ours) FWD KL + LDR-L1 (ours)
GMM	500	FWD KL	2.850 \pm 0.061	77.76 \pm 6.90	
		FWD KL (PATH GRADIENTS)	2.812 \pm 0.008	77.97 \pm 5.32	
	1000	FWD KL + LDR-L2 (OURS)	2.736 \pm 0.003	95.26 \pm 2.48	
		FWD KL + LDR-L1 (OURS)	2.734 \pm 0.004	96.98 \pm 0.60	
ALANINE DIPEPTIDE	1 \times 10 ⁶ *	FWD KL	2.791 \pm 0.013	86.47 \pm 1.43	
		FWD KL (PATH GRADIENTS)	2.777 \pm 0.027	86.82 \pm 5.43	
		FWD KL + LDR-L2 (OURS)	2.725 \pm 0.001	98.62 \pm 0.31	
		FWD KL + LDR-L1 (OURS)	2.727 \pm 0.004	96.83 \pm 2.60	
	5 \times 10 ⁶ *	FWD KL	-214.378 \pm 0.000	87.94 \pm 0.06	
		FWD KL + LDR-L2 (OURS)	-214.432 \pm 0.001	98.25 \pm 0.11	
		FWD KL + LDR-L1 (OURS)	-214.430 \pm 0.000	97.81 \pm 0.07	
		FWD KL	-214.417 \pm 0.001	94.96 \pm 0.14	
ALANINE HEXAPEPTIDE	1 \times 10 ⁶ *	FWD KL	-504.675 \pm 0.002	13.10 \pm 0.11	
		FWD KL + LDR-L2 (OURS)	-504.632 \pm 0.016	14.92 \pm 0.23	
		FWD KL + LDR-L1 (OURS)	-504.759 \pm 0.013	16.35 \pm 0.10	
		FWD KL	-505.174 \pm 0.005	29.60 \pm 0.25	
	5 \times 10 ⁶ *	FWD KL + LDR-L2 (OURS)	-505.259 \pm 0.010	38.70 \pm 0.55	
		FWD KL + LDR-L1 (OURS)	-505.308 \pm 0.007	39.59 \pm 0.44	
		FWD KL	-505.174 \pm 0.005	29.60 \pm 0.25	
		FWD KL + LDR-L2 (OURS)	-505.259 \pm 0.010	38.70 \pm 0.55	

* We note that we performed $> 1 \times 10^9$ target evaluations in the MD simulations used to construct the listed datasets via downsampling (Appendix B.4).

4.2. Training on Unbiased Datasets

We start with the most straightforward setup, training on an unbiased dataset that follows the target distribution and includes target energy labels, $\mathcal{D}_n = \{(x_1, E(x_1)), \dots, (x_n, E(x_n))\}$, $x_i \stackrel{\text{i.i.d.}}{\sim} p_X$. Datasets to train Boltzmann generators are typically obtained from MD simulations, so target energy values already have to be computed during dataset creation. We can therefore apply energy regularization without extra cost.

To test the effect of LDR in different data regimes, we train on both alanine dipeptide and alanine hexapeptide using datasets of increasing size, i.e. 1×10^6 , 2×10^6 and 5×10^6 samples. As a baseline, we use forward KL training without regularization, and compare it against models trained with LDR-L1 and LDR-L2 regularization.

In addition to the molecular benchmarks, we include a simple 2D Gaussian mixture model. Here, we provide path gradients forward KL (Vaitl et al., 2023) as an additional baseline, which uses gradients of the target density. Our attempts to include the path gradient forward KL as an additional baseline also for the experiments on molecular systems in internal coordinates were not successful; we include a detailed discussion and analysis in Appendix D.4.

Results Our results for training on unbiased datasets are summarized in Table 1. Across all three tasks, we observe significant improvements in both NLL and ESS when using

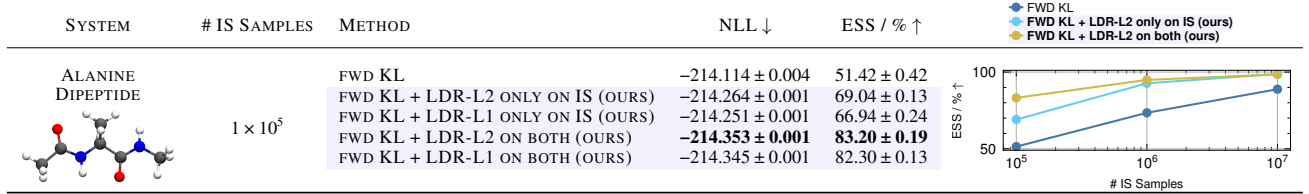
LDR compared to the baselines. For the Gaussian mixture task, LDR regularization allows stable training on only 500 data points, while the performance without LDR significantly degrades for this dataset size. For alanine dipeptide, LDR using 1×10^6 samples outperforms training without LDR with 5×10^6 samples, indicating more than 5 times higher data efficiency. For alanine hexapeptide, we observe that LDR yields the largest improvements for 2×10^6 and 5×10^6 training samples (ESS plot on the right of Table 1). For 1×10^6 , the model likely remains too far from the target, leading to high-variance importance weights and a noisy LD objective, making it least effective in this regime. Moreover, LDR-L1 performs better than LDR-L2 for hexapeptide, consistent with the L1 objective being less sensitive to outliers.

4.3. Training on Biased Datasets

Unbiased molecular dynamics simulations become prohibitively expensive when the relevant configuration space is separated by large free-energy barriers or characterized by slow collective modes. In such regimes, trajectories can remain trapped in metastable regions for long times, making it infeasible to obtain sufficient equilibrium samples from p_X within reasonable computational budgets.

By relaxing the requirement for unbiased samples, biased simulation techniques accelerate exploration by modifying the sampling dynamics, trading exact sampling from p_X for improved state-space coverage (Abrams & Bussi, 2013).

Table 2. Results for training on biased datasets with importance sampling (IS). We show results for pure data-based training with FWD KL, FWD KL + LDR on the IS samples only, and FWD KL + LDR on both the IS samples and the original biased dataset. We report negative log-likelihood (NLL; lower is better) and effective sample size (ESS; higher is better), averaged over 4 independent experiments with standard deviations. **Bold** indicates methods whose performance is not statistically significantly different from the best-performing method (two-sided Welch’s t-test with $p \geq 0.05$). Right: ESS as a function of the number of samples drawn for importance sampling.



The resulting datasets are drawn from a biased distribution p_X^{biased} but are often orders of magnitude cheaper to obtain than unbiased equilibrium data.

We train Boltzmann generators on biased simulation data using a two-stage procedure. First, we perform standard data-based training, using the forward KL on a biased dataset $\mathcal{D}_n^{\text{biased}} = \{x_i\}_{i=1}^n, x_i \sim p_X^{\text{biased}}$. This yields an initial proposal distribution $q_X^{\theta_1}$ that approximates the biased distribution. We use the same pre-trained model $q_X^{\theta_1}$ for all methods.

Second, we generate samples $x_j \sim q_X^{\theta_1}$ and compute importance weights $w(x_j) = \tilde{p}_X(x_j)/q_X^{\theta_1}(x_j)$. From this, we construct an approximate equilibrium dataset $\mathcal{D}_m^{\text{IS}}$ via categorical resampling, i.e., by drawing samples with probabilities proportional to $w(x_j)$.

We then refine our initial biased proposal $q_X^{\theta_1}$ by training on $\mathcal{D}_m^{\text{IS}}$. Here, we compare standard forward KL training on $\mathcal{D}_m^{\text{IS}}$ with its LDR-L1-regularized and LDR-L2-regularized variants. This form of self-refinement has been previously used in other contexts (Schopmans & Friederich, 2025; Tan et al., 2025b). Since LDR can be evaluated over arbitrary reference distributions, we can use not only $\mathcal{D}_m^{\text{IS}}$ for LDR, but also a mixture of $\mathcal{D}_m^{\text{IS}}$ and the biased dataset $\mathcal{D}_n^{\text{biased}}$ (we use a 50 : 50 mixture). This leverages additional training signal from the biased distribution, which is typically difficult to incorporate into Boltzmann generator training.

Dataset To test our methodology of training on biased datasets, we use short trajectories starting in the main modes of the energy landscape of alanine dipeptide. The short runtime of each trajectory leads to high correlations across trajectories, ultimately resulting in a heavily biased dataset of 1×10^6 samples. Details can be found in Appendix 6.

In total, the MD used to generate this biased dataset took only 1.1×10^6 target evaluations and can be performed in < 200 s on a regular laptop. This is in contrast to typical MD simulations, which require $> 1 \times 10^8$ steps for high-quality unbiased datasets for alanine dipeptide (our ground truth MD simulation took ~ 2 days to simulate).

Results Results for training on the biased dataset of alanine dipeptide are summarized in Table 2. Using only 1×10^5 importance samples, LDR applied on $\mathcal{D}_m^{\text{IS}}$ substantially improves performance compared to the non-regularized baseline. Applying regularization on both $\mathcal{D}_m^{\text{IS}}$ and the original biased dataset $\mathcal{D}_n^{\text{biased}}$ further improves performance, leading to a substantial gap. LDR effectively leverages information from the biased data distribution, leading to substantially improved refinement compared to standard importance-sampling-based self-refinement.

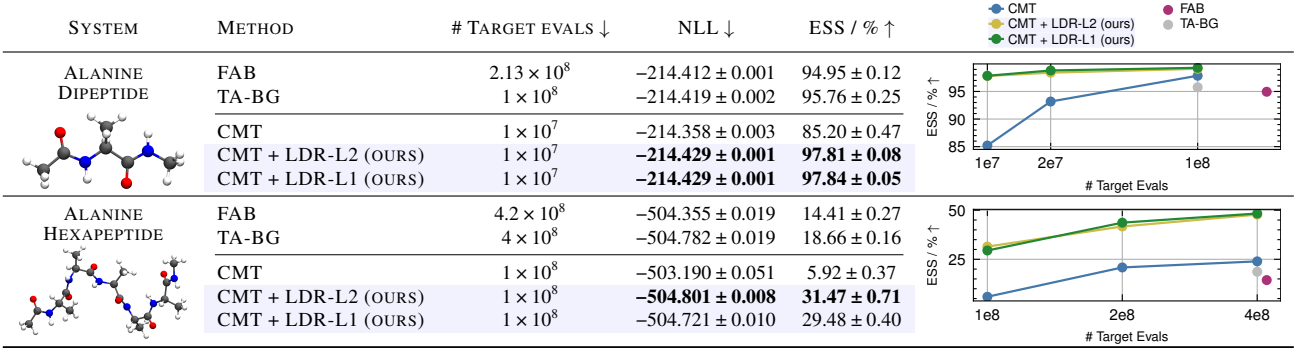
In total, LDR allows training of a well-performing Boltzmann generator using only $1 \times 10^5 + 1.1 \times 10^6$ (to construct the biased dataset) target evaluations. To achieve similar performance, non-regularized training requires more than 10 times more IS samples.

4.4. Variational Training without Target Data

Finally, we show that regularizing data-based training also improves efficiency in the purely variational setting, where no target data (unbiased or biased) is available and training uses only target energy evaluations. Several recent methods train Boltzmann generators by annealing the model distribution toward the target through a sequence of intermediate distributions q_i (Schopmans & Friederich, 2025; von Klitzing et al., 2025). To learn each intermediate distribution q_i , a buffer is built by reweighting model samples to the current intermediate distribution. Standard data-based training is then performed on each buffer until the next intermediate distribution is constructed, so we can readily apply LDR.

Temperature-Annealed Boltzmann Generator (TA-BG) (Schopmans & Friederich, 2025) pre-trains with the reverse Kullback-Leibler (KL) divergence at an elevated temperature and subsequently anneals the model distribution using a number of intermediate temperatures $q_i \propto \tilde{p}_X^{\alpha_i}$. Constrained Mass Transport (CMT) (von Klitzing et al., 2025) extends this idea and uses a generalized annealing path of the form $q_i \propto q_0^{1-\lambda_i} (\tilde{p}_X^{\alpha_i})^{\lambda_i}$. The parameter schedule (λ_i) is chosen adaptively based on a trust-region constraint that limits the KL-difference between subsequent intermediate

Table 3. Results for variational training without access to target data, using only the target energy evaluations. We report negative log-likelihood (NLL; lower is better) and effective sample size (ESS; higher is better). We average over 4 independent experiments with standard deviations for alanine dipeptide, and 3 independent experiments for alanine hexapeptide to limit computational cost. For each number of target evaluations, **bold** indicates methods whose performance is not statistically significantly different from the best-performing method (two-sided Welch’s t-test with $p \geq 0.05$). Right: ESS as a function of the number of target energy evaluations.



distributions. This guarantees sufficient overlap between successive intermediates and improves performance compared to TA-BG. We provide a more detailed introduction to the annealing-based variational framework used in TA-BG and CMT in Appendix B.2. We additionally include Flow Annealed Importance Sampling Bootstrap (FAB), which was the first to successfully learn alanine dipeptide variationally without mode collapse.

LDR can be applied to FAB, TA-BG, and CMT, as all use buffered off-policy training. Since CMT represents the current state of the art, we apply LDR only to CMT. For FAB and TA-BG, we run baseline experiments without LDR. All methods use the same number of gradient descent steps.

CMT provides a particularly suitable environment for applying LDR: by limiting the KL-divergence between intermediate distributions, it enforces sufficient overlap, which stabilizes the resulting log importance weights. This yields a lower-variance learning signal for log-dispersion than, e.g., in our experiments directly on unbiased datasets.

Results Table 3 summarizes our results of applying LDR to variational training with CMT. LDR substantially improves the performance of CMT for all tested settings of total target evaluations. The gap becomes especially pronounced when reducing the number of target evaluations. On alanine dipeptide, CMT + LDR achieves comparable performance using only 1×10^7 target evaluations as CMT with 1×10^8 target evaluations. This indicates an approximately 10 times higher efficiency in terms of target evaluations.

CMT on alanine hexapeptide was originally reported with 4×10^8 target evaluations. In this setting, LDR substantially improves final performance, increasing ESS by more than 20 percentage points. When lowering the number of target evaluations down to 1×10^8 , vanilla CMT shows significant

mode collapse and reaches an ESS of only 5.92 %. In contrast, LDR makes it possible to still achieve stable training in this setting, achieving an ESS of over 30 %. We further note that FAB and TA-BG perform considerably worse, even though they use ≥ 4 times the number of target evaluations.

Overall, LDR allowed us to significantly reduce the number of target evaluations used in CMT while largely preserving final performance. We refer to Appendix D.3 for an ablation where we reduce the number of target evaluations even further than what we report in our main experiments.

4.5. Training Using Cartesian Coordinates

To show that the gains from LDR are not tied to internal coordinate representations, we additionally train Boltzmann generators directly on Cartesian coordinates. To match the data regime used in related works, we used 1×10^5 training samples (Tan et al., 2025a). We use an autoregressive normalizing flow based on a transformer with causal masking (Zhai et al., 2025), adapted to Boltzmann generators by Tan et al. (2025a). Following (Tan et al., 2025a), we incorporate the symmetries via data augmentation (random rotations and center-of-mass noise after centering), and thus train the flow in an augmented space. When estimating unbiased quantities via importance sampling, this requires a correction to map back to the target space; we propose an improved version of this correction compared to the one introduced by Tan et al. (2025a) (see Appendix C.1 for a derivation).

We note that this discrete normalizing flow operating on Cartesian coordinates is substantially faster than continuous normalizing flow or diffusion-based counterparts used in related works. In Appendix B.1, we provide a detailed inference-speed comparison demonstrating that TarFlow achieves nearly a $4000\times$ higher sampling throughput than a representative continuous normalizing flow baseline.

Results Table 4 summarizes our results on Cartesian coordinates. First, we observe that our improved augmentation correction improves results from the original formulation (Tan et al., 2025a). Furthermore, LDR outperforms non-regularized forward KL by a substantial margin. Both LDR-L2 and LDR-L1 perform similarly well. We provide a detailed discussion of these results in Appendix C.2. There, we also provide a comparison with the path gradient version of the forward KL as an additional baseline (Vaitl et al., 2023). Our results show that LDR provides a strong additional training signal from energy labels also in the Cartesian-coordinate setting. While we focused on a controlled single-system benchmark, future work can explore training through LDR in the transferable setting (Tan et al., 2025b).

Table 4. Results for training on Cartesian coordinates using an unbiased dataset from the target distribution of alanine dipeptide. We average over 4 independent experiments with standard deviations. **Bold** indicates methods whose performance is not statistically significantly different from the best-performing method (two-sided Welch’s t-test with $p \geq 0.05$).

METHOD	NLL \downarrow	ESS / % \uparrow
FWD KL (Tan et al., 2025a)	-219.583 ± 0.051	19.40 ± 0.80
FWD KL *	-219.583 ± 0.050	27.32 ± 1.28
FWD KL * + LDR-L2 (OURS)	-219.815 ± 0.034	35.89 ± 1.69
FWD KL * + LDR-L1 (OURS)	-219.800 ± 0.044	35.75 ± 1.63

* Uses our improved augmentation correction, see Appendix C.1.

5. Discussion

While we focus on normalizing flows due to their accuracy and efficient importance sampling, LDR applies to any likelihood-based model class. It can also be applied to diffusion-based Boltzmann generators by reformulating Equation 4 over joint diffusion paths rather than terminal marginals, which upper-bounds the terminal objective (Sanokowski et al., 2025). While variational on-policy log-variance training for diffusion models is well-studied (Richter & Berner, 2023; Sendera et al., 2024), using it as off-policy regularization, as in this manuscript, has not been explored. However, we consider this outside the scope of the current manuscript.

Finally, we emphasize the strong dependence of final performance on dataset size observed across all experiments. The largest unbiased datasets used in this work (5×10^6 samples) are considerably larger than those employed in related studies. We consistently observe substantial performance improvements when increasing dataset size beyond the regimes explored in prior work, both with and without LDR. This suggests that dataset size is a critical factor for Boltzmann generator training. Importantly, while LDR does not remove this dependence, it mitigates it by increasing data efficiency: models trained with LDR experience

significantly improved metrics at smaller dataset sizes.

We evaluated two variants of LDR, LDR-L1 and LDR-L2. Across all benchmarks, both variants yield comparable and substantial performance gains, indicating that the benefits of LDR are robust to the specific choice of dispersion measure. We observe a slight advantage of LDR-L1 in the unbiased training of alanine hexapeptide, which we attribute to the heavy-tailed distribution of importance weights in this high-dimensional energy landscape. By penalizing absolute rather than squared deviations, LDR-L1 is less sensitive to outliers and therefore provides more stable optimization in this regime. Overall, however, the performance difference between LDR-L1 and LDR-L2 remains small, suggesting that either variant is a reasonable default choice in practice.

Limitations A limitation of log-dispersion regularization is the introduction of an additional hyperparameter in form of the relative loss weighting between LDR and the data-based objective. However, we observe only moderate sensitivity to this choice: as shown in Figure 4 in the appendix, performance remains stable over a range of loss weights.

A second limitation is that applying LDR with reference distributions far from the target may cause unstable training. Although this did not occur in our experiments, understanding LDR’s behavior under increasingly biased references is an important direction for future work.

6. Conclusion

We introduced **off-policy log-dispersion regularization (LDR)**, a simple yet powerful framework for incorporating target energy information into the training of Boltzmann generators. By generalizing the log-variance objective and using it as an off-policy shape regularizer, LDR provides an additional training signal without requiring extra on-policy samples and target energy evaluations.

Across a wide range of settings, including training on unbiased equilibrium data, biased simulation datasets, and purely variational training without access to target samples, LDR consistently improves both final performance and data efficiency. In several benchmarks, these gains translate into order-of-magnitude reductions in the number of samples or target energy evaluations required to reach a given performance level. Importantly, the framework is broadly applicable and easy to integrate into existing pipelines.

Reproducibility Statement

The source code to reproduce our experiments will soon be made publicly available on GitHub. We will further publish the ground truth simulation data required for evaluation and training.

Acknowledgments

H.S. acknowledges financial support by the German Research Foundation (DFG) through the Research Training Group 2450 “Tailored Scale-Bridging Approaches to Computational Nanoscience”. P.F. acknowledges funding from the Klaus Tschira Stiftung gGmbH (SIMPLAIX project) and the pilot program Core-Informatics of the Helmholtz Association (KiKIT project). Parts of this work were performed on the HoreKa supercomputer funded by the Ministry of Science, Research and the Arts Baden-Württemberg and by the Federal Ministry of Education and Research. The authors gratefully acknowledge the Gauss Centre for Supercomputing e.V. (www.gauss-centre.eu) for funding this project by providing computing time through the John von Neumann Institute for Computing (NIC) on the GCS Supercomputer JUWELS at Jülich Supercomputing Centre (JSC).

References

Abdin, O. and Kim, P. M. Direct conformational sampling from peptide energy landscapes through hypernetwork-conditioned diffusion. *Nat Mach Intell*, pp. 1–12, June 2024. ISSN 2522-5839. doi: 10.1038/s42256-024-00860-4.

Abrams, C. and Bussi, G. Enhanced Sampling in Molecular Dynamics Using Metadynamics, Replica-Exchange, and Temperature-Acceleration. *Entropy*, 16(1):163–199, December 2013. ISSN 1099-4300. doi: 10.3390/e16010163.

Akhound-Sadegh, T., Lee, J., Bose, A. J., Bortoli, V. D., Doucet, A., Bronstein, M. M., Beaini, D., Ravanbakhsh, S., Neklyudov, K., and Tong, A. Progressive Inference-Time Annealing of Diffusion Models for Sampling from Boltzmann Densities, June 2025.

Alder, B. J. and Wainwright, T. E. Studies in Molecular Dynamics. I. General Method. *J. Chem. Phys.*, 31(2): 459–466, August 1959. ISSN 0021-9606. doi: 10.1063/1.1730376.

Blessing, D., Jia, X., Esslinger, J., Vargas, F., and Neumann, G. Beyond ELBOs: A Large-Scale Evaluation of Variational Methods for Sampling. In *Forty-First International Conference on Machine Learning*, June 2024.

Choi, J., Chen, Y., Tao, M., and Liu, G.-H. Non-equilibrium Annealed Adjoint Sampler. In *The Thirty-ninth Annual Conference on Neural Information Processing Systems*, October 2025.

Conor Durkan, Artur Bekasov, Iain Murray, and George Papamakarios. Nflows: Normalizing flows in PyTorch, November 2020.

Dibak, M., Klein, L., Krämer, A., and Noé, F. Temperature steerable flows and Boltzmann generators. *Phys. Rev. Res.*, 4(4):L042005, October 2022. doi: 10.1103/PhysRevResearch.4.L042005.

Dinh, L., Sohl-Dickstein, J., and Bengio, S. Density estimation using Real NVP, February 2017.

Durkan, C., Bekasov, A., Murray, I., and Papamakarios, G. Neural Spline Flows. In *Advances in Neural Information Processing Systems*, volume 32. Curran Associates, Inc., 2019.

Eastman, P., Galvelis, R., Peláez, R. P., Abreu, C. R. A., Farr, S. E., Gallicchio, E., Gorenko, A., Henry, M. M., Hu, F., Huang, J., Krämer, A., Michel, J., Mitchell, J. A., Pande, V. S., Rodrigues, J. P., Rodriguez-Guerra, J., Simmonett, A. C., Singh, S., Swails, J., Turner, P., Wang, Y., Zhang, I., Chodera, J. D., De Fabritiis, G., and Markland, T. E. OpenMM 8: Molecular Dynamics Simulation with Machine Learning Potentials. *J. Phys. Chem. B*, 128(1):109–116, January 2024. ISSN 1520-6106. doi: 10.1021/acs.jpcb.3c06662.

Hollingsworth, S. A. and Dror, R. O. Molecular Dynamics Simulation for All. *Neuron*, 99(6):1129–1143, September 2018. ISSN 0896-6273. doi: 10.1016/j.neuron.2018.08.011.

Jing, B., Corso, G., Chang, J., Barzilay, R., and Jaakkola, T. S. Torsional Diffusion for Molecular Conformer Generation. In *Advances in Neural Information Processing Systems*, October 2022.

Jing, B., Berger, B., and Jaakkola, T. AlphaFold Meets Flow Matching for Generating Protein Ensembles. In *Proceedings of the 41st International Conference on Machine Learning*, pp. 22277–22303. PMLR, July 2024.

Kim, J. C., Bloore, D., Kapoor, K., Feng, J., Hao, M.-H., and Wang, M. Scalable Normalizing Flows Enable Boltzmann Generators for Macromolecules, January 2024.

Kim, M., Seong, K., Woo, D., Ahn, S., and Kim, M. On scalable and efficient training of diffusion samplers, May 2025.

Kingma, D. P. and Ba, J. Adam: A Method for Stochastic Optimization, January 2017.

Klein, L. and Noé, F. Transferable Boltzmann Generators. In *The Thirty-eighth Annual Conference on Neural Information Processing Systems*, November 2024.

Klein, L., Krämer, A., and Noé, F. Equivariant flow matching, June 2023.

Lewis, S., Hempel, T., Jiménez-Luna, J., Gastegger, M., Xie, Y., Foong, A. Y. K., Satorras, V. G., Abdin, O., Veeling, B. S., Zaporozhets, I., Chen, Y., Yang, S., Schneuing, A., Nigam, J., Barbero, F., Stimper, V., Campbell, A., Yim, J., Lienen, M., Shi, Y., Zheng, S., Schulz, H., Munir, U., Clementi, C., and Noé, F. Scalable emulation of protein equilibrium ensembles with generative deep learning, December 2024.

Liu, G.-H., Choi, J., Chen, Y., Miller, B. K., and Chen, R. T. Q. Adjoint Schrödinger Bridge Sampler, June 2025.

Martino, L., Elvira, V., and Louzada, F. Effective Sample Size for Importance Sampling based on discrepancy measures. *Signal Processing*, 131:386–401, February 2017. ISSN 01651684. doi: 10.1016/j.sigpro.2016.08.025.

Metropolis, N., Rosenbluth, A. W., Rosenbluth, M. N., Teller, A. H., and Teller, E. Equation of State Calculations by Fast Computing Machines. *J. Chem. Phys.*, 21(6):1087–1092, June 1953. ISSN 0021-9606. doi: 10.1063/1.1699114.

Midgley, L. I., Stimper, V., Simm, G. N. C., Schölkopf, B., and Hernández-Lobato, J. M. Flow Annealed Importance Sampling Bootstrap. In *The Eleventh International Conference on Learning Representations*, September 2022.

Midgley, L. I., Stimper, V., Antorán, J., Mathieu, E., Schölkopf, B., and Hernández-Lobato, J. M. SE(3) Equivariant Augmented Coupling Flows. In *Thirty-Seventh Conference on Neural Information Processing Systems*, August 2023.

Noé, F. Bgflow. AI4Science group, FU Berlin (Frank Noé and co-workers), December 2024.

Noé, F., Olsson, S., Köhler, J., and Wu, H. Boltzmann generators: Sampling equilibrium states of many-body systems with deep learning. *Science*, 365(6457):eaaw1147, September 2019. doi: 10.1126/science.aaw1147.

Paszke, A., Gross, S., Massa, F., Lerer, A., Bradbury, J., Chanan, G., Killeen, T., Lin, Z., Gimelshein, N., Antiga, L., Desmaison, A., Köpf, A., Yang, E., DeVito, Z., Raison, M., Tejani, A., Chilamkurthy, S., Steiner, B., Fang, L., Bai, J., and Chintala, S. PyTorch: An Imperative Style, High-Performance Deep Learning Library, December 2019.

Peng, X. and Gao, A. Flow perturbation to accelerate Boltzmann sampling. *Nat Commun*, 16(1):6604, July 2025. ISSN 2041-1723. doi: 10.1038/s41467-025-62039-8.

Rehman, D., Akhound-Sadegh, T., Gazizov, A., Bengio, Y., and Tong, A. FALCON: Few-step Accurate Likelihoods for Continuous Flows, December 2025a.

Rehman, D., Davis, O., Lu, J., Tang, J., Bronstein, M., Bengio, Y., Tong, A., and Bose, A. J. Efficient Regression-Based Training of Normalizing Flows for Boltzmann Generators, October 2025b.

Rehman, D., Davis, O., Lu, J., Tang, J., Bronstein, M., Bengio, Y., Tong, A., and Bose, A. J. FORT: Forward-Only Regression Training of Normalizing Flows, June 2025c.

Rezende, D. J., Papamakarios, G., Racaniere, S., Albergo, M., Kanwar, G., Shanahan, P., and Cranmer, K. Normalizing Flows on Tori and Spheres. In *Proceedings of the 37th International Conference on Machine Learning*, pp. 8083–8092. PMLR, November 2020.

Richter, L. and Berner, J. Improved sampling via learned diffusions. In *The Twelfth International Conference on Learning Representations*, October 2023.

Richter, L., Boustati, A., Nüsken, N., Ruiz, F. J. R., and Akyildiz, Ö. D. VarGrad: A Low-Variance Gradient Estimator for Variational Inference, October 2020.

Rissanen, S., OuYang, R., He, J., Chen, W., Heinonen, M., Solin, A., and Hernández-Lobato, J. M. Progressive Tempering Sampler with Diffusion. In *Forty-Second International Conference on Machine Learning*, June 2025.

Sanokowski, S., Bartmann, C., Gruber, L., Hochreiter, S., and Lehner, S. Rethinking the Training of Diffusion Bridge Samplers: Losses and Exploration. In *Frontiers in Probabilistic Inference: Learning Meets Sampling*, April 2025.

Satorras, V. G., Hoogeboom, E., Fuchs, F. B., Posner, I., and Welling, M. E(n) Equivariant Normalizing Flows, January 2022.

Schopmans, H. and Friederich, P. Conditional Normalizing Flows for Active Learning of Coarse-Grained Molecular Representations. In *Forty-First International Conference on Machine Learning*, June 2024.

Schopmans, H. and Friederich, P. Temperature-Annealed Boltzmann Generators. In *Proceedings of the 42nd International Conference on Machine Learning*, pp. 53467–53500. PMLR, October 2025.

Sendera, M., Kim, M., Mittal, S., Lemos, P., Scimeca, L., Rector-Brooks, J., Adam, A., Bengio, Y., and Malkin, N. Improved off-policy training of diffusion samplers. In *The Thirty-eighth Annual Conference on Neural Information Processing Systems*, November 2024.

Stimper, V., Schölkopf, B., and Hernandez-Lobato, J. M. Resampling Base Distributions of Normalizing Flows. In *Proceedings of The 25th International Conference*

on Artificial Intelligence and Statistics, pp. 4915–4936.
PMLR, May 2022.

Sugita, Y. and Okamoto, Y. Replica-exchange molecular dynamics method for protein folding. *Chemical Physics Letters*, 314(1):141–151, November 1999. ISSN 0009-2614. doi: 10.1016/S0009-2614(99)01123-9.

Tan, C. B., Bose, J., Lin, C., Klein, L., Bronstein, M. M., and Tong, A. Scalable Equilibrium Sampling with Sequential Boltzmann Generators. In *Forty-Second International Conference on Machine Learning*, June 2025a.

Tan, C. B., Hassan, M., Klein, L., Syed, S., Beaini, D., Bronstein, M. M., Tong, A., and Neklyudov, K. Amortized Sampling with Transferable Normalizing Flows, August 2025b.

Vaitl, L. and Klein, L. Path Gradients after Flow Matching, May 2025.

Vaitl, L., Winkler, L., Richter, L., and Kessel, P. Fast and unified path gradient estimators for normalizing flows. In *The Twelfth International Conference on Learning Representations*, October 2023.

von Klitzing, C., Blessing, D., Schopmans, H., Friederich, P., and Neumann, G. Learning Boltzmann Generators via Constrained Mass Transport, October 2025.

Wahl, S., Rousselot, A., Draxler, F., and Koethe, U. TRADE: Transfer of Distributions between External Conditions with Normalizing Flows. In *The 28th International Conference on Artificial Intelligence and Statistics*, February 2025.

Zhai, S., Zhang, R., Nakkiran, P., Berthelot, D., Gu, J., Zheng, H., Chen, T., Bautista, M. A., Jaitly, N., and Susskind, J. Normalizing Flows are Capable Generative Models, June 2025.

Zhang, F., Midgley, L. I., and Hernández-Lobato, J. M. Efficient and Unbiased Sampling from Boltzmann Distributions via Variance-Tuned Diffusion Models, May 2025.

Zheng, S., He, J., Liu, C., Shi, Y., Lu, Z., Feng, W., Ju, F., Wang, J., Zhu, J., Min, Y., Zhang, H., Tang, S., Hao, H., Jin, P., Chen, C., Noé, F., Liu, H., and Liu, T.-Y. Predicting equilibrium distributions for molecular systems with deep learning. *Nat Mach Intell*, 6(5):558–567, May 2024. ISSN 2522-5839. doi: 10.1038/s42256-024-00837-3.

A. Theory

A.1. Optimum of Training with Log-Dispersion Objectives

Proposition A.1 (Log-dispersion regularization as a divergence). *Let r_X be a reference distribution with full support on X , i.e., $r_X(x) > 0$ for all $x \in X$. Let $\tilde{p}_X(x) > 0$ be an unnormalized target density and let q_X^θ be a normalized model density with $q_X^\theta(x) > 0$ for all x . Then $\mathcal{L}_{\text{LD}}^{\theta(p)}(r_X) \geq 0$, and*

$$\mathcal{L}_{\text{LD}}^{\theta(p)}(r_X) = 0 \iff q_X^\theta(x) = \frac{\tilde{p}_X(x)}{\mathcal{Z}} = p_X(x).$$

In particular, $\mathcal{L}_{\text{LD}}^{\theta(p)}(r_X)$ is a divergence whose unique minimum is attained at the target distribution.

Proof. Nonnegativity is immediate since $|\cdot|^p \geq 0$.

If $\mathcal{L}_{\text{LD}}^{\theta(p)}(r_X) = 0$, then $|f^\theta(x) - \mathbb{E}_{r_X}[f^\theta(x)]|^p = 0$ r_X -a.s., which implies $f^\theta(x) = c$ r_X -a.s. for $c = \mathbb{E}_{r_X}[f^\theta(x)]$. Because r_X has full support, this equality holds everywhere on X . Thus,

$$\log \frac{\tilde{p}_X(x)}{q_X^\theta(x)} = c \iff q_X^\theta(x) = e^{-c} \tilde{p}_X(x).$$

Normalization of q_X^θ yields

$$1 = \int q_X^\theta(x) dx = e^{-c} \int \tilde{p}_X(x) dx = e^{-c} \mathcal{Z},$$

and therefore $q_X^\theta(x) = \tilde{p}_X(x)/\mathcal{Z} = p_X(x)$.

Conversely, if $q_X^\theta = p_X$, then $f^\theta(x) = \log \mathcal{Z}$ is constant, and hence $\mathcal{L}_{\text{LD}}^{\theta(p)}(r_X) = 0$. \square

A.2. Log-Dispersion Using Reference Distributions without Full Support

The divergence property of the log-dispersion objective established above relies critically on the assumption that the reference distribution r_X has full support on X . In this work, however, we want to use fixed datasets, corresponding to a reference distribution whose support is restricted to a subset of configuration space. In this setting, the divergence property no longer holds.

Proposition A.2 (LD without full support is not a divergence). *Let r_X be a reference distribution whose support $\text{supp}(r_X) \subsetneq X$ is a strict subset of the configuration space. Then $\mathcal{L}_{\text{LD}}^{\theta(p)}(r_X)$ is not a divergence on the space of normalized densities on X . In particular, there exist normalized densities $q_X^\theta \neq p_X$ such that*

$$\mathcal{L}_{\text{LD}}^{\theta(p)}(r_X) = 0.$$

Proof. If $\text{supp}(r_X) \subsetneq X$, then the condition

$$\mathcal{L}_{\text{LD}}^{\theta(p)}(r_X) = 0$$

implies only that $f^\theta(x) = c$ holds r_X -almost surely, i.e., for all $x \in \text{supp}(r_X)$. This yields

$$q_X^\theta(x) = e^{-c} \tilde{p}_X(x) \quad \text{for } x \in \text{supp}(r),$$

but places no constraint on $q_X^\theta(x)$ outside the support of r_X .

As a result, one can modify q_X^θ arbitrarily on $X \setminus \text{supp}(r_X)$ while maintaining normalization, without affecting the value of $\mathcal{L}_{\text{LD}}^{\theta(p)}(r_X)$. Therefore, $\mathcal{L}_{\text{LD}}^{\theta(p)}(r_X) = 0$ does not imply $q_X^\theta = p_X$ on X , and LD fails to be a divergence in this case. Appendix D.2 illustrates this phenomenon empirically. \square

This situation arises naturally when r_X corresponds to an empirical data distribution, e.g., obtained from molecular dynamics simulations, which typically cover only a low-dimensional manifold or a limited region of configuration space. In this regime, LD alone enforces agreement between q_X^θ and p_X only on the data manifold, leaving the model unconstrained elsewhere and allowing incorrect normalization or spurious probability mass outside the data support. Furthermore, also for variational methods such as CMT, were off-policy training on fixed buffers is performed, the divergence property does not hold.

A.3. Consistency of Log-Dispersion Regularization

We now show that combining the log-dispersion objective with a standard data-based divergence resolves this issue and restores the correct optimum even when the reference distribution lacks full support. We call this approach log-dispersion regularization.

Let $\mathcal{L}_{\text{data}}^\theta$ denote a data-based divergence whose unique minimum is attained at the target distribution p_X , such as the forward KL divergence, score matching, or flow matching, depending on the model class. We consider the combined objective

$$\mathcal{L}^\theta = \lambda_{\text{data}} \mathcal{L}_{\text{data}}^\theta + \lambda_{\text{LD}} \mathcal{L}_{\text{LD}}^{\theta(p)}, \quad \lambda_{\text{data}}, \lambda_{\text{LD}} > 0.$$

Proposition A.3 (Consistency of log-dispersion regularization). *Assume that $\mathcal{L}_{\text{data}}^\theta \geq 0$ and that*

$$\mathcal{L}_{\text{data}}^\theta = 0 \iff q_X^\theta = p_X.$$

Then the combined objective \mathcal{L}^θ satisfies

$$\mathcal{L}^\theta \geq 0, \quad \mathcal{L}^\theta = 0 \iff q_X^\theta = p_X,$$

independently of whether the reference distribution used in $\mathcal{L}_{\text{LD}}^{\theta(p)}$ has full support.

Proof. Nonnegativity follows immediately from nonnegativity of both terms and the assumption $\lambda_{\text{data}}, \lambda_{\text{LD}} > 0$.

If $\mathcal{L}^\theta = 0$, then necessarily $\mathcal{L}_{\text{data}}^\theta = 0$, which implies $q_X^\theta = p_X$ by assumption. Conversely, if $q_X^\theta = p_X$, then $\mathcal{L}_{\text{data}}^\theta = 0$ and $f^\theta(x) = \log \mathcal{Z}$ is constant, yielding $\mathcal{L}_{\text{LD}}^{\theta(p)} = 0$ for any reference distribution r_X . Thus $\mathcal{L}^\theta = 0$. \square

This result shows that log-dispersion can be safely employed as a regularization term when evaluated off-policy on a fixed dataset. The data-based objective ensures global correctness and proper normalization of the model distribution, while LDR provides an auxiliary training signal that aligns the learned density with the target energy landscape on the data manifold by reducing dispersion in the log importance weights. As a result, the combined objective preserves the true target distribution as its unique optimum, while benefiting from the additional structure encoded in the target energies.

A.4. Gradients of Log-Dispersion Objectives

We now analyze the gradients of the log-dispersion objectives with respect to the model parameters θ , with particular focus on the cases $p = 1$ and $p > 1$. Our goal is to understand the behavior of these gradients at the optimum $q_X^\theta = p_X$.

Recall that

$$f^\theta(x) = -\log q_X^\theta(x) - \frac{E(x)}{k_B T}, \quad \bar{f}^\theta := \mathbb{E}_{r_X}[f^\theta(x)],$$

and

$$\mathcal{L}_{\text{LD}}^{\theta(p)} = \mathbb{E}_{r_X} [|f^\theta(x) - \bar{f}^\theta|^p].$$

Gradient of the general LD objective Assuming sufficient regularity to interchange gradient and expectation, the gradient of $\mathcal{L}_{\text{LD}}^{\theta(p)}$ is given by

$$\nabla_\theta \mathcal{L}_{\text{LD}}^{\theta(p)} = p \mathbb{E}_{r_X} \left[|f^\theta(x) - \bar{f}^\theta|^{p-1} \text{sign}(f^\theta(x) - \bar{f}^\theta) (\nabla_\theta f^\theta(x) - \mathbb{E}_{r_X}[\nabla_\theta f^\theta(x)]) \right], \quad (7)$$

where $\text{sign}(u) = u/|u|$ for $u \neq 0$, and $\text{sign}(0)$ denotes the subdifferential $[-1, 1]$.

At the optimum $q_X^\theta = p_X$, we have

$$f^\theta(x) = \log \mathcal{Z} \quad \text{for all } x,$$

and therefore $f^\theta(x) - \bar{f}^\theta = 0$ identically. The behavior of the gradient at this point depends critically on the choice of p .

Case $p = 1$: For $p = 1$, the LD objective reduces to

$$\mathcal{L}_{\text{LD}}^{\theta(1)} = \mathbb{E}_{r_X} [|f^\theta(x) - \bar{f}^\theta|],$$

with gradient

$$\nabla_\theta \mathcal{L}_{\text{LD}}^{\theta(1)} = \mathbb{E}_{r_X} [\text{sign}(f^\theta(x) - \bar{f}^\theta) (\nabla_\theta f^\theta(x) - \mathbb{E}_{r_X} [\nabla_\theta f^\theta(x)])]. \quad (8)$$

At the exact optimum, $f^\theta(x) - \bar{f}^\theta = 0$ for all x . However, the subdifferential of the absolute value at zero is the interval $[-1, 1]$, so the gradient is not uniquely defined. In the vicinity of the optimum, when $f^\theta(x) - \bar{f}^\theta$ is small but nonzero, the gradient in (8) remains of constant magnitude, independent of how close q_X^θ is to p_X . This contrasts with $p > 1$, where gradient contributions are smoothly damped as the optimum is approached (see below). Consequently, in stochastic optimization, where the model never exactly reaches $q_X^\theta = p_X$ and residual fluctuations persist, the L1 log-dispersion objective can induce persistent gradient noise near the optimum.

Case $p > 1$: For $p > 1$, the gradient in (7) contains the factor $|f^\theta(x) - \bar{f}^\theta|^{p-1}$. At the optimum, where $f^\theta(x) - \bar{f}^\theta = 0$ identically, this factor vanishes pointwise, since $p - 1 > 0$. Therefore,

$$\nabla_\theta \mathcal{L}_{\text{LD}}^{\theta(p)} = 0 \quad \text{for all } p > 1.$$

As the model distribution approaches the optimum $q_X^\theta = p_X$, the deviations $f^\theta(x) - \bar{f}^\theta$ shrink, and the factor $|f^\theta(x) - \bar{f}^\theta|^{p-1}$ in the gradient increasingly damps gradient contributions. At the optimum, this damping becomes exact, and the gradients of the LD term vanish identically. Consequently, once the model has reached the target distribution, the log-dispersion regularizer induces no further parameter updates.

Implications Although the $p = 1$ objective can be more robust to outliers due to its linear penalty, it may introduce persistent gradient noise near the optimum. In contrast, objectives with $p > 1$ combine vanishing gradients at convergence with increasing sensitivity to large deviations of $f^\theta(x)$ from its mean. This trade-off suggests a natural distinction between the cases $p = 1$ and $p > 1$ when employing log-dispersion regularization in practice.

B. Experimental Setup

B.1. Architecture

Here, we summarize the normalizing flow architectures used in this work. We further show the approximate inference time of each architecture in Table 5. To put the inference times into perspective, we also included a continuous normalizing flow, evaluated by exactly calculating the trace of the Jacobian using the codebase of [Vaitl & Klein \(2025\)](#).

Table 5. Approximate sampling speed for different architecture / system combinations, evaluated including importance weights calculation. For each architecture / system combination, we increased the batch size until either running out of memory or until the throughput did not increase further. Benchmarks were performed on a single NVIDIA A100 GPU (80 GB memory).

SYSTEM	ARCHITECTURE	COORDINATE REPRESENTATION	SAMPLES / HOUR
ALANINE DIPEPTIDE	SPLINE FLOW	ICs	$\sim 2.8 \times 10^8$
ALANINE HEXAPEPTIDE	SPLINE FLOW	ICs	$\sim 1.1 \times 10^8$
ALANINE DIPEPTIDE	TARFLOW	Cartesian	$\sim 2.8 \times 10^7$
ALANINE DIPEPTIDE	EGNN (SATORRAS ET AL., 2022)	Cartesian	~ 7300

GMM To train on the GMM target density, we use a RealNVP architecture ([Dinh et al., 2017](#)) with affine coupling layers. The model consists of 15 coupling layers, each containing a conditioner network implemented as a fully-connected neural network with weight normalization and batch normalization. Each conditioner network has two hidden layers of 160 units with tanh activation functions. The coupling layers alternate their masking pattern to ensure all dimensions are transformed. The base distribution is a standard Gaussian $\mathcal{N}(0, I_2)$.

Molecular systems in internal coordinates The normalizing flow architecture follows established designs used in prior studies (Midgley et al., 2022; Schopmans & Friederich, 2025; 2024). Molecular conformations are represented in internal coordinates consisting of bond lengths, bond angles, and dihedral angles.

The model comprises 8 pairs of neural spline coupling layers based on monotonic rational-quadratic splines (Durkan et al., 2019). Each spline operates on the interval $[0, 1]$ and uses 8 bins. Within each pair of coupling layers, a random binary mask determines which dimensions are transformed and which are conditioned upon in the first layer, while the negated mask is applied in the second layer. Dihedral angle dimensions are handled using circular spline transformations (Rezende et al., 2020) to account for their periodic topology, and a fixed random periodic shift is applied after every coupling layer. The networks producing the spline parameters are fully connected neural networks with hidden layer sizes $[256, 256, 256, 256, 256]$ and ReLU nonlinearities. To encode periodicity, each dihedral angle ψ_i is represented as $(\cos \psi_i, \sin \psi_i)$ when provided as input to the parameter networks.

The base distribution of the flow is chosen as a uniform distribution on $[0, 1]$ for dihedral angles, and a truncated Gaussian on $[0, 1]$ for bond lengths and bond angles, with mean $\mu = 0.5$ and standard deviation $\sigma = 0.1$.

Following Schopmans & Friederich (2025), all internal coordinates are mapped to the $[0, 1]$ domain required by the spline transformations. Dihedral angles are rescaled by division by 2π . Bond lengths and angles are shifted and scaled according to $\eta'_i = (\eta_i - \eta_{i;\min})/\sigma + 0.5$, where $\eta_{i;\min}$ is taken from a minimum-energy configuration obtained via energy minimization. The scaling parameter σ is set to 0.07 nm for bond lengths and to 0.5730 for bond angles.

The molecular systems considered admit two enantiomeric configurations corresponding to L- and R-chirality, whereas naturally occurring structures predominantly exhibit L-chirality. To restrict generated samples to the L-chiral manifold, the output ranges of the splines corresponding to the relevant dihedral angles are constrained as described in Schopmans & Friederich (2025). In addition, certain atoms or functional groups are formally permutation invariant in the force-field energy, but appear in a fixed ordering in molecular dynamics data. Analogously to the chirality constraints, the spline transformations are restricted such that only the permutations observed in the validation data can be generated (Schopmans & Friederich, 2025).

To implement the normalizing flow models on internal coordinate representations, we used the *bgflow* (Noé, 2024) and *nflows* (Conor Durkan et al., 2020) libraries.

Molecular systems in Cartesian coordinates For our experiments on Cartesian coordinates, we leverage TarFlow (Zhai et al., 2025), a block-wise autoregressive normalizing flow based on a transformer architecture with causal masking. We closely follow the hyperparameters introduced by Tan et al. (2025a). We use 4 transformation blocks, each with 4 attention layers and 256 channels. Cartesian coordinates are transformed block-wise, treating the three Cartesian coordinates of each atom as one block.

B.2. Variational Training Based on Annealing Paths

This section provides a short overview of the annealing-based variational sampling approaches CMT (von Klitzing et al., 2025) and TA-BG (Schopmans & Friederich, 2025).

Let $p_X : \mathbb{R}^d \rightarrow \mathbb{R}^+$ be a probability density function known up to its normalization constant \mathcal{Z} , i.e.,

$$p_X(x) = \frac{\tilde{p}_X(x)}{\mathcal{Z}}, \quad \text{with} \quad \mathcal{Z} = \int_{\mathbb{R}^d} \tilde{p}_X(x) dx.$$

A common strategy to generate samples $x \sim p_X(x)$ is to approximate p_X with a parameterized variational model $q_X^\theta \in \mathcal{Q}_\theta \subset \mathcal{P}(\mathbb{R}^d)$ by minimizing the reverse KL divergence,

$$\min_{\theta} D_{\text{KL}}(q_X^\theta \| p_X). \quad (9)$$

While this approach works well for simple target distributions, more complex targets often lead to mode collapse, where some modes of p_X are poorly represented or entirely missed by the model.

Annealing paths One strategy to mitigate this issue is the use of variational annealing paths, which interpolate between an initial model distribution q_0 and the target distribution p_X through a sequence of intermediate densities $(q_i)_{i=1}^K$, with

$q_K = p_X$. Recent work on constrained variational objectives by von Klitzing et al. (2025) (CMT) establishes a connection between a family of constrained variational objectives and common annealing paths. We therefore consider the geometric-tempered annealing path

$$q_i \propto q_0^{1-\lambda_i} (p_X^{1/T_i})^{\lambda_i}, \quad \lambda_i \in \mathbb{R}_{\geq 0}, \quad T_i \in [1, \infty), \quad i = 1 \dots K,$$

proposed by CMT (von Klitzing et al., 2025), which generalizes the widely used geometric annealing path

$$q_i \propto q_0^{1-\lambda_i} p_X^{\lambda_i}, \quad \lambda_i \in \mathbb{R}_{\geq 0}, \quad i = 1 \dots K,$$

and the temperature annealing path

$$q_i \propto p_X^{1/T_i}, \quad T_i \in [1, \infty), \quad i = 1 \dots K,$$

used by TA-BG (Schopmans & Friederich, 2025).

Annealing schedules TA-BG first pre-trains the model at an elevated temperature using the reverse KL objective. Since modes are more interconnected at high temperatures, this helps avoid mode collapse. TA-BG subsequently anneals the model distribution, starting from the high-temperature distribution q_0 , using a manually chosen geometric temperature annealing schedule.

In contrast, CMT (von Klitzing et al., 2025) skips the pre-training phase and directly starts with an uninformed prior distribution q_0 . von Klitzing et al. (2025) then derive a geometric-tempered annealing path and its adaptive schedule by analytically solving the constrained variational objective

$$q_{i+1} = \arg \min_{q_X \in \mathcal{P}(\mathbb{R}^d)} D_{\text{KL}}(q_X \| p_X) \quad \text{s.t.} \quad D_{\text{KL}}(q_X \| q_i) \leq \varepsilon_{\text{tr}}, \quad \mathcal{H}(q_i) - \mathcal{H}(q_X) \leq \varepsilon_{\text{ent}}, \quad \int q_X(x) \, dx = 1$$

for general probability measures $q \in \mathcal{P}(\mathbb{R}^d)$. While this approach can adaptively choose both $(\lambda_i)_i$ (trust-region constraint) and $(T_i)_i$ (entropy constraint), we found it simpler to select the temperature schedule manually, as in TA-BG, while still enforcing the trust-region constraint. Using a manual temperature schedule thus yields the objective

$$q_{i+1} = \arg \min_{q_X \in \mathcal{P}(\mathbb{R}^d)} D_{\text{KL}}(q_X \| p_X^{1/T_{i+1}}) \quad \text{s.t.} \quad D_{\text{KL}}(q_X \| q_i) \leq \varepsilon_{\text{tr}}, \quad \int q_X(x) \, dx = 1.$$

In our experiments, performance remained stable, although decreases may occur in other settings.

Algorithm 1 Annealing algorithm

Require: Initial density q_0 , target density \tilde{p}_X , divergence D , approximation family \mathcal{Q}_θ

for $i \leftarrow 1, \dots, K$ **do**

 Initialize buffer \mathcal{B}_i with samples from current model q_X^θ

 Prepare for next intermediate target q_i (e.g., choose λ_i adaptively, compute importance weights, ...)

for $k \leftarrow 1, \dots, L$ **do**

 Update q_X^θ by performing gradient descent on $D(q_i, q_X^\theta)$ using the buffer \mathcal{B}_i

end for

end for

return $q_X^\theta \approx p_X$

Algorithm Given an annealing path and schedule, the original objective in Equation (9) breaks down into a sequence of simpler variational objectives

$$\min_{\theta} D(q_i, q_X^\theta), \quad i = 1 \dots K,$$

where D denotes a statistical divergence. Both CMT and TA-BG employ the forward Kullback-Leibler divergence.

Both variational approaches follow a nested optimization structure, consisting of an outer and an inner loop. In each outer iteration, a buffer of samples is generated and then used off-policy to update the model parameters during the inner loop. We can thus readily apply LDR in this setting. An abstract version of the annealing algorithm is provided in Algorithm 1.

Table 6. Summary of the molecular systems considered in this study, along with the associated force field parametrizations. To be consistent with prior work, we consider two different force-field variants for alanine dipeptide. The first is used for our experiments in internal coordinates, while the latter is used for the experiments in Cartesian coordinates.

NAME	NO. ATOMS	SEQUENCE	FORCE FIELD	CONSTRAINTS
ALANINE DIPEPTIDE	22	ACE-ALA-NME	Amber ff96 with OBC1 implicit solvation	NONE
ALANINE DIPEPTIDE	22	ACE-ALA-NME	Amber f99SBildn with Amber99 OBC implicit solvation	NONE
ALANINE HEXAPEPTIDE	62	ACE-5-ALA-NME	Amber f99SBildn with Amber99 OBC implicit solvation	HYDROGEN BOND LENGTHS

B.3. Target Densities

GMM target We use a Gaussian mixture model (GMM) in $d = 2$ dimensions, closely following the system introduced by [Vaitl et al. \(2023\)](#). The target distribution is defined as an equally-weighted mixture of 2^d Gaussian components arranged on a regular grid. The component means are positioned at the vertices of a hypercube with coordinates $\mu_i \in \{-1, +1\}^d$, resulting in $2^2 = 4$ modes located at $(\pm 1, \pm 1)$. Each component is an independent isotropic Gaussian with standard deviation $\sigma = 0.5$.

Molecular systems All our experiments on molecular systems were performed at 300 K. An overview of the molecular systems investigated in this work, together with the corresponding force field parametrizations, is provided in Table 6. All energy evaluations used for model training were carried out with OpenMM version 8.0.0 ([Eastman et al., 2024](#)) on the CPU platform, employing 18 parallel workers.

In line with previous studies ([Midgley et al., 2022](#); [Schopmans & Friederich, 2025](#); [von Klitzing et al., 2025](#)), we employ a regularized energy formulation to mitigate excessively large van der Waals contributions arising from atomic overlaps:

$$E_{\text{reg}}(E) = \begin{cases} E, & \text{if } E \leq E_{\text{high}}, \\ \log(E - E_{\text{high}} + 1) + E_{\text{high}}, & \text{if } E_{\text{high}} < E \leq E_{\text{max}}, \\ \log(E_{\text{max}} - E_{\text{high}} + 1) + E_{\text{high}}, & \text{if } E > E_{\text{max}}. \end{cases} \quad (10)$$

We choose $E_{\text{high}} = 1 \times 10^8$ and $E_{\text{max}} = 1 \times 10^{20}$, following the values reported by [Midgley et al. \(2022\)](#).

Table 7. Summary of the number of trainable parameters for each architecture / system combination.

SYSTEM	ARCHITECTURE	COORDINATE REPRESENTATION	NO. PARAMETERS
GMM	REALNVP	-	403 230
ALANINE DIPEPTIDE	SPLINE FLOW	ICs	7 421 512
ALANINE HEXAPEPTIDE	SPLINE FLOW	ICs	12 124 616
ALANINE DIPEPTIDE	TARFLOW	Cartesian	12 668 952

B.4. Datasets

We performed extensive molecular dynamics simulations to obtain high-quality ground truth datasets for both training and evaluation. Our simulation protocol builds on that reported by [Schopmans & Friederich \(2025\)](#) and [von Klitzing et al. \(2025\)](#).

For all molecular systems, we performed two independent simulations: The first was used to build a training dataset with 5×10^6 samples and a validation dataset of 1×10^6 samples, the second to build a test dataset with 1×10^7 samples. The validation dataset was used to optimize hyperparameters, and the test dataset to report the final metrics.

Alanine dipeptide For alanine dipeptide, we performed molecular dynamics simulations with the OpenMM integrator *LangevinMiddle* and a time step of 1 fs. We first equilibrated for 200 ns, followed by the production simulation of 5 μ s.

Alanine hexapeptide For alanine hexapeptide, we performed replica-exchange molecular dynamics (Sugita & Okamoto, 1999) simulations on the temperatures [300.0 K, 332.27 K, 368.01 K, 407.60 K, 451.44 K, 500.0 K] with the OpenMM integrator *LangevinMiddle* and a time step of 1 fs. We first equilibrated each replica independently for 200 ns without exchanges, then equilibrated for 200 ns with exchanges, and subsequently performed the production simulation of 2 μ s per replica. To build our datasets, the data of the 300.0 K replica was used.

Biased dataset for alanine dipeptide To produce the biased dataset for alanine dipeptide (see Section 4.3 of the main text), we used 4 starting configurations located in the main minima of the energy surface of alanine dipeptide, see Figure 2. In each configuration, we started 20 MD trajectories at 300 K, each with a length of 13750 steps and time step 1 fs using a *LangevinMiddle* integrator. We discarded the first 1250 steps of each trajectory. Since we recorded every step of the trajectories, this resulted in a biased dataset with 1×10^6 samples.

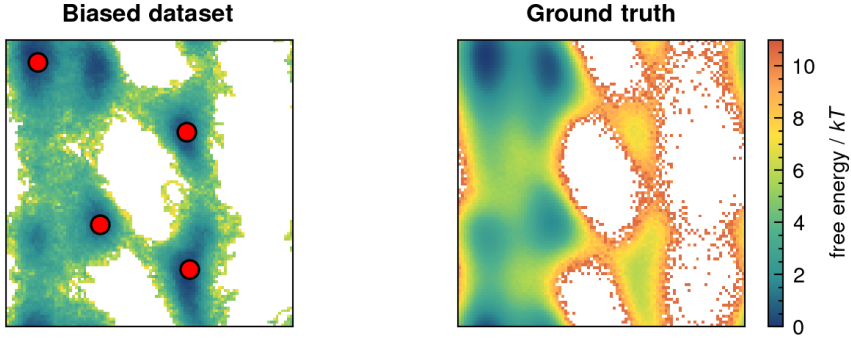


Figure 2. Ramachandran plot of the biased training dataset for alanine dipeptide. The four starting configurations of the trajectories are labeled in red. Due to the short length of the trajectories, the high-energy metastable states on the right side are oversampled compared to the ground truth.

B.5. Metrics

As discussed in the main part of our manuscript, we use the negative log-likelihood (NLL) and ESS as the main metrics of our experiments. We also introduce several additional metrics below. All metrics were estimated using 1×10^7 samples from the model and ground truth (when needed). For the experiments in Cartesian coordinates with TarFlow, we used 1×10^6 samples for evaluation due to the reduced inference speed.

NLL The NLL is defined as

$$\text{NLL} = -\mathbb{E}_{x \sim p_X(x)} [\log q_X^\theta(x)] . \quad (11)$$

For the experiments on Cartesian coordinates with data augmentation, we evaluate the NLL on the augmented distribution $p_{\text{aug}}(x)$, as this is ultimately the one learned by the model (see Appendix C.1 for details).

ESS The ESS can be calculated using the following equation (Martino et al., 2017; Midgley et al., 2023):

$$\text{ESS} = \frac{n_{\text{e,rv}}}{N} = \frac{1}{N \sum_{i=1}^N \bar{w}(x_i)^2} \quad (12)$$

with $x_i \sim q_X^\theta(x_i)$, $\bar{w}(x_i) = \frac{w(x_i)}{\sum_{j=1}^N w(x_j)}$, $w(x) = \frac{\tilde{p}_X(x)}{q_X^\theta(x)}$

To calculate the ESS, the top 0.01 % of importance weights were truncated to their minimum value within this subset, following previous work (Midgley et al., 2022; Schopmans & Friederich, 2025; von Klitzing et al., 2025). This clipping is performed to remove outliers due to model instabilities from the importance weights. The effective sample size was computed using the regularized energy function (Equation 10).

Ramachandran metrics Ramachandran plots visualize the two-dimensional log-density of the joint distribution of backbone dihedral angle pairs (ϕ, ψ) in a peptide. They capture the dominant conformational degrees of freedom of molecular systems and are particularly sensitive to mode collapse and missing high-energy regions.

To quantitatively assess deviations between ground-truth and model-generated Ramachandran plots, we follow previous work (Midgley et al., 2022; Schopmans & Friederich, 2025; von Klitzing et al., 2025) and compute the forward Kullback–Leibler divergence between the discretized ground truth Ramachandran distribution and the model distribution, which we call **RAM KL**. Both distributions were estimated using 100×100 bins over the full dihedral angle range. Since alanine hexapeptide has 5 pairs of backbone dihedral angles, we average over the 5 corresponding **RAM KL** metrics.

In addition, we report a reweighted variant of this metric (**RAM KL w. RW**), where model samples are first reweighted to the target distribution using importance weights before constructing the Ramachandran histogram. To improve the numerical stability of the reweighted estimate and to suppress the influence of rare outliers caused by model instabilities, the same clipping procedure as used for the ESS computation is applied: the top 0.01 % of importance weights are clipped to the minimum value within this subset.

TICA metrics Time-lagged independent component analysis (TICA) provides a low-dimensional representation of the slow collective degrees of freedom of molecular systems. Distributions in TICA space are therefore sensitive to deficiencies in the learned slow dynamics and to mode collapse in kinetically relevant regions.

To quantitatively assess deviations between ground-truth and model-generated distributions in TICA space, we compute the forward Kullback–Leibler divergence between the discretized ground truth TICA distribution and the model distribution, which we call **TICA KL**. Both distributions were estimated using 100×100 bins over the TICA ranges determined from the ground-truth samples and using the first two TICA components.

In addition, we report a reweighted variant of this metric (**TICA KL w. RW**), where model samples are first reweighted to the target distribution using importance weights before constructing the TICA histogram, using the same importance weight clipping as used for **RAM KL w. RW**.

Metrics based on energy distribution In line with related work (Tan et al., 2025a), we further measure the discrepancy between generated and reference target energy distributions by computing the 2-Wasserstein distance between their one-dimensional distributions over potential energy values (estimated from samples). Lower $\mathcal{E}\mathcal{W}_2$ indicates a closer match of the generated energy histogram to the reference. Since this metric is very sensitive to outliers, in line with related work, we only report this metric after categorical resampling of the flow sample distribution according to the importance weights. For our experiments in internal coordinates, we use 1×10^7 flow samples and resample to 1×10^7 samples. For our experiments in Cartesian coordinates, we use 1×10^6 flow samples and resample to 1×10^6 samples. We note that, in contrast to Wasserstein distances in $d > 1$, they can be efficiently calculated even for very large sample sizes in 1D.

We emphasize that this histogram energy metric compares only a one-dimensional marginal distribution, and can therefore be less informative than metrics such as ESS, which more directly reflects the quality of the reweighting and the match to the target distribution. Moreover, across all our experiments the reweighted energy histograms are already very close to the target; hence, $\mathcal{E}\mathcal{W}_2$ mainly captures small residual fluctuations, and we caution against placing too much weight on small differences in this metric.

Further metrics used in related work Several related works report the torus Wasserstein distance ($\mathbb{T}\mathcal{W}_2$) on backbone dihedral angles and the Wasserstein distance in the TICA projection space, $\text{TICA-}\mathcal{W}_2$ (Tan et al., 2025a;b; Rehman et al., 2025c; von Klitzing et al., 2025; Rehman et al., 2025a;b).

This metric is typically estimated using 10^4 samples (some more recent works use up to 2.5×10^5 samples), where the sample-based dihedral angle distribution can still be a very coarse proxy for the underlying target distribution; for example, even in the two-dimensional Ramachandran marginals of alanine dipeptide, the qualitative appearance changes drastically as the number of reference samples increases from 10^4 to 10^7 (Figure 3). Especially to properly resolve the high-energy

metastable region on the right side of the Ramachandran, which is crucial to be sensitive with respect to mode collapse, a large number of samples is necessary. Increasing the number of samples to match the 10^7 samples we use for the metrics **RAM KL** and **TICA KL** would make Wasserstein-based evaluation prohibitively expensive, particularly when considering higher-dimensional torus products for longer peptides such as alanine hexapeptide.

For these reasons, we focus on our KL-based metrics, which can be estimated reliably at very large sample sizes, and that we found to yield more stable and reliable comparisons.

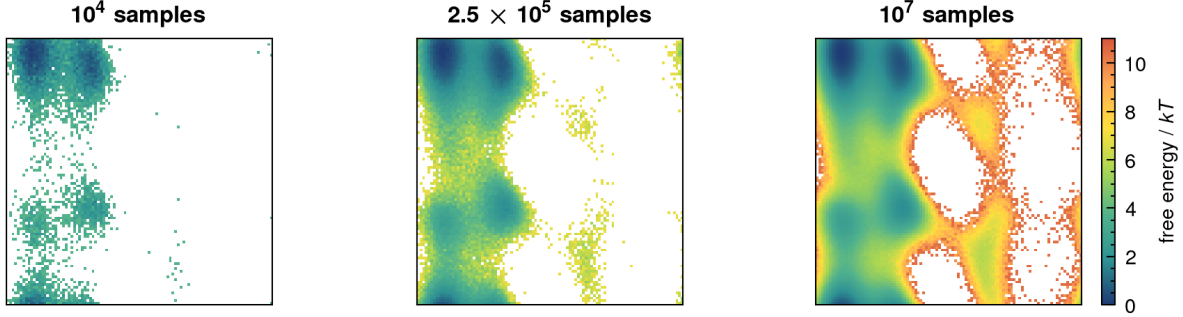


Figure 3. Ramachandran plots for alanine dipeptide, using randomly chosen 1×10^4 samples (left), 2.5×10^5 (middle), and 1×10^7 samples (right) from the ground truth dataset.

B.6. Hyperparameters

General All experiments were performed using the Adam optimizer (Kingma & Ba, 2017) and were implemented in PyTorch (Paszke et al., 2019). All experiments included a cosine annealing learning rate scheduler with a single cycle.

Initial learning rates were tuned separately for each experiment, using a logarithmically spaced grid search. We first evaluated a coarse grid spanning several orders of magnitude, and subsequently refined the search around the best-performing region using a finer grid of the form $\{\dots, 10^{-4}, 3.2 \times 10^{-5}, 10^{-5}, \dots\}$.

All data-based training methods (unbiased and biased) used a batch size of 1024.

The total number of gradient descent steps for each method can be found in Table 8.

LDR To report best-case performance with LDR, we tuned λ_{data} over the grid $\{0.1, 0.3, 0.5, 0.7, \dots\}$ while fixing $\lambda_{\text{LD}} = 1$ for the experiments in internal coordinates. We emphasize, however, that LDR performs well across a range of choices of λ_{data} , as shown in Figure 4. For the experiments in Cartesian coordinates, we set $\lambda_{\text{data}} = 1$ and tuned λ_{LD} over the grid $\{0.1, 0.3, 0.5, 0.7, \dots\}$.

CMT We used a batch size of 1000 for alanine dipeptide and 2000 for alanine hexapeptide. Gradient norm clipping was applied with a threshold of 100. At the start of training, the learning rate was linearly warmed up over the first 1000 steps. The trust-region bound was set to 0.3 for all experiments.

For alanine dipeptide, we used 200 outer annealing steps, while 400 annealing steps were used for alanine hexapeptide. To compute the number of samples for the buffer in each annealing step, we uniformly distributed the total number of target energy evaluations over the number of annealing steps.

As described in Section B.2, we did not use the entropy constraint introduced by von Klitzing et al. (2025). Instead, we chose a manual geometric temperature schedule that geometrically anneals the temperature from 1200 K to 300 K over the first half of the total number of gradient descent steps. With this fixed schedule, we observed CMT to achieve comparable results as when using an entropy constraint. In this setup, CMT is very similar to TA-BG with an additional trust-region constraint to improve overlap of consecutive distributions.

TA-BG For our experiments with TA-BG, we started from the exact hyperparameters specified by Schopmans & Friederich (2025). We refer to (Schopmans & Friederich, 2025) for details. Reverse KL pre-training was performed at 1200 K, from where a geometric annealing path to 300 K was followed. To ensure a fair comparison, we matched the number of gradient descent steps used in TA-BG to those used in CMT (see Table 8).

FAB For our experiments with FAB, we used the exact hyperparameters specified by von Klitzing et al. (2025), without additional tuning.

B.7. Training Times

We summarize the total training time (excluding evaluation) observed on an NVIDIA A100 GPU (40 GB memory) for each method in Table 8. We emphasize that LDR does not change the required training time and can be added with no extra cost.

Table 8. Summary of the number of gradient descent steps and the total training time (excluding evaluation) for each method.

SYSTEM	ARCHITECTURE (REP.)	METHOD	NO. GRADIENT STEPS	TRAINING TIME
GMM	REALNVP	UNBIASED DATASET	10 000	~ 4 min
ALANINE DIPEPTIDE	SPLINE FLOW (IC)	UNBIASED DATASET	250 000	~ 11.8 h
ALANINE HEXAPEPTIDE	SPLINE FLOW (IC)	UNBIASED DATASET	250 000	~ 17.3 h
ALANINE DIPEPTIDE	SPLINE FLOW (IC)	BIASED DATASET	250 000	~ 12.6 h
ALANINE DIPEPTIDE	SPLINE FLOW (IC)	CMT (1×10^7 EVALS)	400 000	~ 17.9 h
ALANINE HEXAPEPTIDE	SPLINE FLOW (IC)	CMT (1×10^8 EVALS)	800 000	~ 53.0 h
ALANINE DIPEPTIDE	TARFLOW (CART.)	UNBIASED DATASET	400 000	~ 18.6 h

C. Training on Cartesian Coordinates

C.1. Augmentation

Directly enforcing translational and rotational invariance of the target distribution within a discrete normalizing flow architecture is challenging due to inherent architectural constraints of normalizing flows. As a result, Tan et al. (2025a) adopt an alternative strategy and train a non-invariant flow, while accounting for these symmetries through data augmentation as follows:

1. Let $X = \mathbb{R}^{N \times 3}$. For a sample $x \in X$, define

$$\bar{x} := \frac{1}{N} \sum_{i=1}^N x_i, \quad x^\circ := x - \mathbf{1}\bar{x}^\top.$$

2. Define the augmentation map

$$s : X_0 \times \mathbb{R}^3 \rightarrow X, \quad s(x^\circ, t) = x^\circ + \mathbf{1}t^\top.$$

3. Sample an independent translation:

$$t \sim \mathcal{N}(0, \sigma_t^2 I_3).$$

4. Apply the augmentation (push-forward):

$$x_{\text{aug}} = s(x^\circ, t) = x^\circ + \mathbf{1}t^\top$$

Note: While molecular dynamics (MD) simulations, in principle, explore all possible molecular rotations due to the rotation-invariance of p_X , in practice, we additionally apply randomly sampled rotations during training, which increases sample diversity and robustness.

Adding noise to the center of mass is crucial. Without this noise, the data distribution lies on a $3N - 3$ -dimensional submanifold of \mathbb{R}^{3N} . As a result, any mapping from a full-dimensional base distribution would require a singular Jacobian, violating the invertibility assumptions of normalizing flows.

In the following, we derive the push-forward density $p_{\text{aug}}(x)$ of the augmentation scheme described above.

Lemma C.1 (Center-of-mass augmentation). *Let p_{X_0} be a probability density on the centered subspace*

$$X_0 := \{z \in X : \bar{z} = 0\},$$

assume p_{X_0} is rotation invariant, i.e., $p_{X_0}(zR) = p_{X_0}(z)$ for all $R \in \text{SO}(3)$, and let $t \sim \mathcal{N}(0, \sigma_t^2 I_3)$.

The augmented density $p_{\text{aug}}(x)$ on the full space X , given by the push-forward using the map s , is, up to normalization:

$$p_{\text{aug}}(x) \propto p_{X_0}(x^\circ) \mathcal{N}(\bar{x} \mid 0, \sigma_t^2 I_3).$$

Proof. We begin with the joint density of the independent variables $x^\circ \in X_0, t \in \mathbb{R}^3$:

$$p(x^\circ, t) = p_{X_0}(x^\circ) \mathcal{N}(t \mid 0, \sigma_t^2 I_3).$$

A change-of-variables of this joint distribution using the map $s(x^\circ, t) = x$ leads to an augmented distribution on the full space, given by

$$p_{\text{aug}}(x) = p(s^{-1}(x)) \cdot |\det J|^{-1} \quad \text{with} \quad J = \frac{\partial s}{\partial(x^\circ, t)}$$

Substituting the joint density expression and the transformation, we obtain:

$$p_{\text{aug}}(x) \propto p_{X_0}(x - \mathbf{1}\bar{x}^\top) \mathcal{N}(\bar{x} \mid 0, \sigma_t^2 I_3) \cdot |\det J|^{-1}$$

Since s is a linear transformation, its Jacobian determinant is constant. This leaves us with

$$p_{\text{aug}}(x) \propto p_{X_0}(x^\circ) \mathcal{N}(\bar{x} \mid 0, \sigma_t^2 I_3),$$

which completes the proof. \square

Augmented loss functions We can now express the augmented versions of both the forward KL and the LD objective using the non-augmented target distribution $p_{X_0}(x)$ as

$$\min_{\theta} D_{\text{KL}}(p_{\text{aug}} \| q_X^\theta) = \min_{\theta} -\mathbb{E}_{p_{\text{aug}}(x)} [\log q_X^\theta(x)] = \min_{\theta} \mathbb{E}_{\substack{x \sim p_{X_0} \\ t \sim \mathcal{N}(0, \sigma_t^2 I_3)}} [\log q_X^\theta(x^\circ + \mathbf{1}t^\top)]$$

and

$$\min_{\theta} \mathcal{L}_{\text{LD}}^{\theta(p)} = \min_{\theta} \mathbb{E}_{p_{\text{aug}}(x)} [|f^\theta(x) - \mathbb{E}_{p_{\text{aug}}(x)} [f^\theta(x)]|^p] = \min_{\theta} \mathbb{E}_{\substack{x \sim p_{X_0} \\ t \sim \mathcal{N}(0, \sigma_t^2 I_3)}} [|f^\theta(x^\circ, t) - \mathbb{E}_{\substack{x \sim p_{X_0} \\ t \sim \mathcal{N}(0, \sigma_t^2 I_3)}} [f^\theta(x^\circ, t)]|^p],$$

with

$$f^\theta(x^\circ, t) = \log \tilde{p}_{X_0}(x^\circ) + \log \mathcal{N}(t \mid 0, \sigma_t^2 I_3) - \log q_X^\theta(x^\circ + \mathbf{1}t^\top).$$

Importance sampling correction Using the loss functions above, the normalizing flow learns to model the augmented distribution $p_{\text{aug}}(x)$, rather than the (non-augmented) target density p_{X_0} . To account for this during importance sampling with respect to p_{X_0} , Tan et al. (2025a) introduced the following correction of the proposal density:

$$\log q_X^{\theta c}(x) = \log q_X^\theta(x) + \frac{\|\bar{x}\|^2}{2\sigma_t^2} - \log \left[\frac{\|\bar{x}\|^2}{\sqrt{2}\sigma_t^3 \Gamma(\frac{3}{2})} \right] \quad (13)$$

This correction effectively removes a χ_3 distribution from the proposal density.

However, as shown above, the augmented density that the normalizing flow learns factorizes as

$$p_{\text{aug}}(x) \propto p_{X_0}(x^\circ) \mathcal{N}(\bar{x} \mid 0, \sigma_t^2 I_3). \quad (14)$$

Consequently, the discrepancy between the learned proposal and the target density arises solely from the additional Gaussian factor in the augmented coordinates. A natural correction, therefore, consists of explicitly removing this Gaussian contribution from the proposal density, yielding

$$\log q_X^{\theta c}(x) = \log q_X^\theta(x) - \log \mathcal{N}(\bar{x} \mid 0, \sigma_t^2 I_3) \quad (15)$$

This recovers a proposal density consistent with importance sampling toward p_{X_0} . Our results show empirically that this correction yields improved results compared to the one proposed by [Tan et al. \(2025a\)](#) (Table 4 and Table 13).

C.2. Extended Discussion of Results

As mentioned in the main text, we also used the path-gradient estimator for the forward KL objective as a baseline in our Cartesian-coordinate experiments; we provide additional details here. For this method, we relied on the “plug-and-play” implementation provided by [Vaitl et al. \(2023\)](#). In our setup, this implementation was approximately $4\times$ slower per optimizer step than the other training objectives considered. To match the overall computational budget, we therefore ran path-gradient forward KL for only 100 000 optimizer steps, whereas the other methods were trained for 400 000 steps.

Despite this constraint, we do observe the characteristic low-variance behavior of path-gradient forward KL: when measured as a function of the number of gradient updates, it tends to converge faster than the alternatives. However, this advantage does not translate to improved performance as a function of wall-clock time in our experiments, due to its substantially higher per-step cost.

We note that [Vaitl & Klein \(2025\)](#) addressed a closely related issue in the context of continuous normalizing flows—where the computational gap is much more pronounced—by first pre-training with flow matching and then fine-tuning with path gradients. However, to keep the experimental setup simple, we did not include pre-training and fine-tuning pipelines in our setting.

Finally, we emphasize that path-gradient forward KL is not a direct competitor to LDR. Conceptually, path-gradient forward KL regularizes training through the inclusion of target *gradients*, whereas LDR regularizes through the inclusion of target *energy values*. These mechanisms are complementary and could be readily combined in future work.

D. Additional Experiments

D.1. Sensitivity to Loss Weights

Compared to standard data-based training, our method introduces an additional hyperparameter that scales the two loss components relative to each other. We visualize the sensitivity of the final model performance on the choice of the hyperparameter λ_{data} in Figure 4. For each chosen λ_{data} , we tune the learning rate separately to remove confounding effects caused by non-optimal settings. As one can see, both LDR-L1 and LDR-L2 outperform the baseline without regularization across a large range of chosen λ_{data} . Furthermore, LDR-L1 appears somewhat more stable with respect to λ_{data} compared to LDR-L2.

D.2. Training without a Data-Based Objective

As outlined in Section A, LDR needs to be combined with a divergence that ensures correct normalization of the proposal. Figure 5 illustrates what happens when only LDR (here, LDR-L1) is used for training on an unbiased dataset. While the proposal matches the dataset where the dataset has support, it is unconstrained outside of the data manifold.

The same problem occurs when running CMT (as well as TA-BG) with only LDR. Both methods build buffers by reweighting model samples to an intermediate target distribution. Since the LDR objective is evaluated over this reweighted fixed dataset while training on each buffer, the same problem exists.

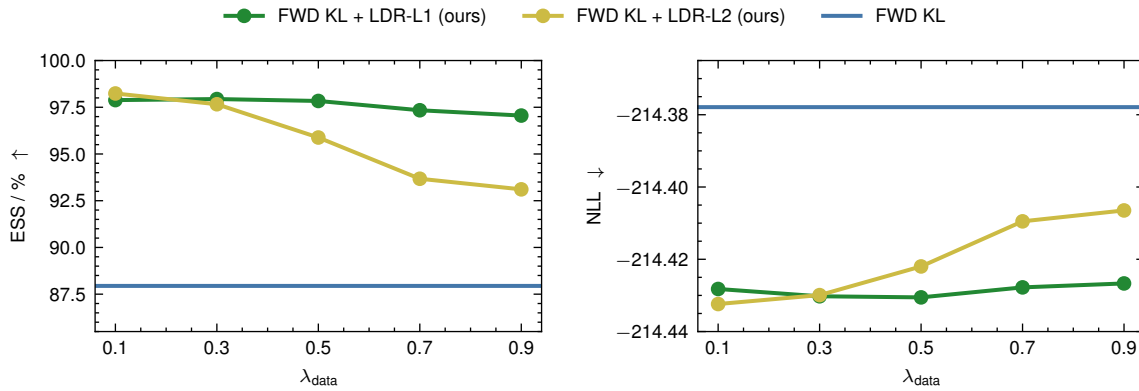


Figure 4. Final ESS and NLL as a function of the loss weight λ_{data} for unbiased training on alanine dipeptide using 1×10^6 samples.

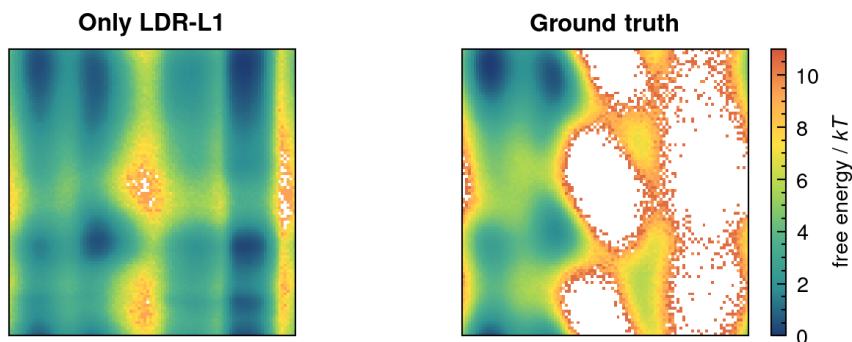


Figure 5. Ramachandran obtained for alanine dipeptide when training with only LDR-L1, without an additional data-based divergence.

D.3. Pushing the Limits of CMT

The LDR objective introduces an additional training signal, enabling effective variational training with substantially fewer gradient descent steps and total target energy evaluations. While our main experiments use 1×10^7 target evaluations as the lowest setting of CMT for alanine dipeptide, this ablation further reduces the evaluation budget.

Figure 6 reports the final performance of CMT, CMT + LDR-L1, and CMT + LDR-L2 under a linear scaling of both the number of gradient descent steps and the buffer size per annealing step, while fixing the number of annealing steps at 200. Although performance degrades as the training budget is reduced, CMT with log-dispersion regularization is significantly more robust to fewer gradient descent steps and target energy evaluations than non-regularized CMT. In particular, CMT + LDR-L1 reaches a final ESS of 82.98 % in approximately 130 minutes of wall-clock time on an NVIDIA A100 GPU (40 GB memory) using only 10^6 target energy evaluations. Non-regularized CMT yields very poor performance in this setting.

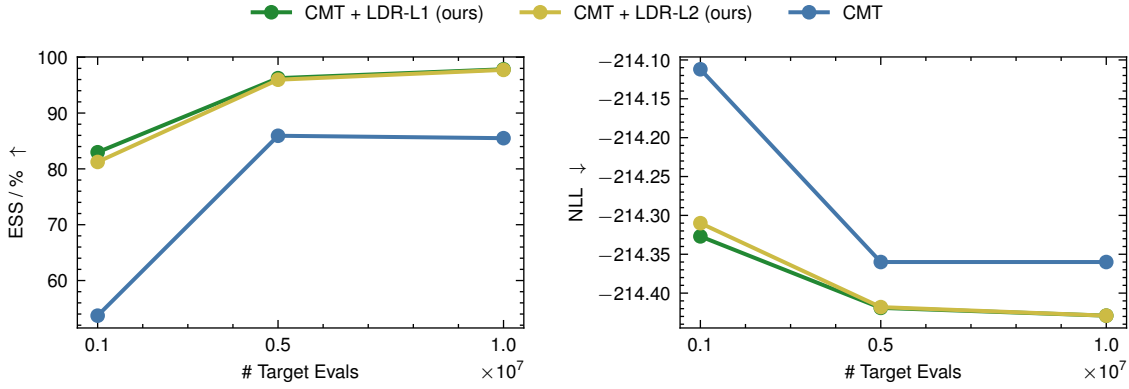


Figure 6. Final ESS and NLL for a total of 10^6 , 5×10^6 , and 10^7 energy evaluations.

D.4. Path Gradient Forward KL with Neural Spline Flows

While we provide baseline experiments with the path gradient formulation of the forward KL (Vaitl et al., 2023; Vaitl & Klein, 2025) on the Gaussian mixture system and on alanine dipeptide using Cartesian coordinates, we did not manage to achieve stable training on internal coordinates with neural spline flows. We tested several variants of gradient norm clipping and tuned the learning rate extensively. We hypothesize that the problem lies in the non-continuity of the gradients of the log-density of the neural spline flow (due to the periodic handling of torsion angles), which makes regularization using gradients of the target density difficult.

E. Extended Results

Table 9. Results for training on unbiased datasets from the target distribution of the GMM system. We average over 4 independent experiments with standard deviations. For each number of samples, **bold** indicates methods whose performance is not statistically significantly different from the best-performing method (two-sided Welch's t-test with $p \geq 0.05$).

SYSTEM	# SAMPLES	METHOD	NLL ↓	ESS / % ↑
GMM	500	FWD KL	2.850 ± 0.061	77.76 ± 6.90
		FWD KL (PATH GRADIENTS)	2.812 ± 0.008	77.97 ± 5.32
		FWD KL + LDR-L2 (OURS)	2.736 ± 0.003	95.26 ± 2.48
		FWD KL + LDR-L1 (OURS)	2.734 ± 0.004	96.98 ± 0.60
GMM	1000	FWD KL	2.791 ± 0.013	86.47 ± 1.43
		FWD KL (PATH GRADIENTS)	2.777 ± 0.027	86.82 ± 5.43
		FWD KL + LDR-L2 (OURS)	2.725 ± 0.001	98.62 ± 0.31
		FWD KL + LDR-L1 (OURS)	2.727 ± 0.004	96.83 ± 2.60
GMM	10000	FWD KL	2.733 ± 0.003	96.75 ± 0.46
		FWD KL (PATH GRADIENTS)	2.726 ± 0.002	97.54 ± 1.44
		FWD KL + LDR-L2 (OURS)	2.730 ± 0.014	97.54 ± 2.50
		FWD KL + LDR-L1 (OURS)	2.720 ± 0.001	99.47 ± 0.29

Table 10. Results for training on unbiased datasets from the target distribution of alanine dipeptide and alanine hexapeptide. We average over 4 independent experiments with standard deviations. For each number of samples, **bold** indicates methods whose performance is not statistically significantly different from the best-performing method (two-sided Welch's t-test with $p \geq 0.05$).

SYSTEM	# SAMPLES	METHOD	NLL ↓	ESS / % ↑	RAM KL ↓	RAM KL W. RW ↓	TICA KL ↓	TICA KL W. RW ↓	$\mathcal{E} \cdot \mathcal{W}_2$
ALANINE DIPEPTIDE	1×10^6	FWD KL	-214.378 ± 0.000	87.94 ± 0.06	(2.57 ± 0.12) $\times 10^{-3}$	(1.96 ± 0.04) $\times 10^{-3}$	(1.18 ± 0.18) $\times 10^{-3}$	(1.05 ± 0.07) $\times 10^{-3}$	(5.99 ± 1.47) $\times 10^{-3}$
		FWD KL + LDR-L2 (OURS)	-214.432 ± 0.001	98.25 ± 0.11	(1.60 ± 0.05) $\times 10^{-3}$	(1.34 ± 0.03) $\times 10^{-3}$	(9.58 ± 0.20) $\times 10^{-4}$	(7.05 ± 0.34) $\times 10^{-4}$	(4.96 ± 0.64) $\times 10^{-3}$
		FWD KL + LDR-L1 (OURS)	-214.430 ± 0.000	97.81 ± 0.07	(1.64 ± 0.04) $\times 10^{-3}$	(1.55 ± 0.03) $\times 10^{-3}$	(9.71 ± 0.91) $\times 10^{-4}$	(8.40 ± 0.87) $\times 10^{-4}$	(5.88 ± 0.51) $\times 10^{-3}$
ALANINE DIPEPTIDE	2×10^6	FWD KL	-214.396 ± 0.001	91.06 ± 0.22	(1.79 ± 0.05) $\times 10^{-3}$	(1.68 ± 0.06) $\times 10^{-3}$	(8.74 ± 0.48) $\times 10^{-4}$	(9.21 ± 0.42) $\times 10^{-4}$	(6.32 ± 1.93) $\times 10^{-3}$
		FWD KL + LDR-L2 (OURS)	-214.435 ± 0.001	98.80 ± 0.11	(1.42 ± 0.04) $\times 10^{-3}$	(1.18 ± 0.04) $\times 10^{-3}$	(9.10 ± 0.94) $\times 10^{-4}$	(6.51 ± 0.31) $\times 10^{-4}$	(6.32 ± 1.17) $\times 10^{-3}$
		FWD KL + LDR-L1 (OURS)	-214.435 ± 0.000	98.81 ± 0.04	(1.48 ± 0.02) $\times 10^{-3}$	(1.36 ± 0.04) $\times 10^{-3}$	(8.62 ± 0.49) $\times 10^{-4}$	(7.18 ± 0.34) $\times 10^{-4}$	(6.00 ± 1.86) $\times 10^{-3}$
ALANINE DIPEPTIDE	5×10^6	FWD KL	-214.417 ± 0.001	94.96 ± 0.14	(1.49 ± 0.02) $\times 10^{-3}$	(1.42 ± 0.03) $\times 10^{-3}$	(7.21 ± 0.20) $\times 10^{-4}$	(7.17 ± 0.32) $\times 10^{-4}$	(5.83 ± 1.54) $\times 10^{-3}$
		FWD KL + LDR-L2 (OURS)	-214.437 ± 0.000	99.04 ± 0.02	(1.34 ± 0.03) $\times 10^{-3}$	(1.28 ± 0.03) $\times 10^{-3}$	(7.87 ± 0.42) $\times 10^{-4}$	(6.92 ± 0.26) $\times 10^{-4}$	(5.23 ± 0.44) $\times 10^{-3}$
		FWD KL + LDR-L1 (OURS)	-214.437 ± 0.001	99.09 ± 0.12	(1.38 ± 0.04) $\times 10^{-3}$	(1.29 ± 0.04) $\times 10^{-3}$	(7.94 ± 0.13) $\times 10^{-4}$	(6.91 ± 0.26) $\times 10^{-4}$	(6.37 ± 1.06) $\times 10^{-3}$
ALANINE HEXAPEPTIDE	1×10^6	FWD KL	-504.675 ± 0.002	13.10 ± 0.11	(3.38 ± 0.52) $\times 10^{-3}$	(6.50 ± 0.18) $\times 10^{-3}$	(4.47 ± 0.60) $\times 10^{-3}$	(1.04 ± 0.06) $\times 10^{-3}$	(6.93 ± 0.93) $\times 10^{-2}$
		FWD KL + LDR-L2 (OURS)	-504.632 ± 0.016	14.92 ± 0.23	(1.29 ± 0.09) $\times 10^{-2}$	(4.31 ± 0.04) $\times 10^{-3}$	(2.37 ± 0.22) $\times 10^{-2}$	(7.01 ± 0.30) $\times 10^{-3}$	(4.75 ± 1.19) $\times 10^{-2}$
		FWD KL + LDR-L1 (OURS)	-504.759 ± 0.013	16.35 ± 0.10	(5.04 ± 0.30) $\times 10^{-3}$	(4.89 ± 0.13) $\times 10^{-3}$	(8.49 ± 0.40) $\times 10^{-3}$	(7.86 ± 0.23) $\times 10^{-3}$	(5.52 ± 1.54) $\times 10^{-2}$
ALANINE HEXAPEPTIDE	2×10^6	FWD KL	-504.813 ± 0.008	16.33 ± 0.19	(3.06 ± 0.10) $\times 10^{-3}$	(5.80 ± 0.17) $\times 10^{-3}$	(4.29 ± 0.23) $\times 10^{-3}$	(9.36 ± 0.26) $\times 10^{-3}$	(5.67 ± 0.56) $\times 10^{-2}$
		FWD KL + LDR-L2 (OURS)	-505.034 ± 0.007	25.13 ± 0.24	(3.66 ± 0.17) $\times 10^{-3}$	(3.26 ± 0.03) $\times 10^{-3}$	(5.95 ± 0.38) $\times 10^{-3}$	(5.24 ± 0.09) $\times 10^{-3}$	(5.17 ± 0.69) $\times 10^{-2}$
		FWD KL + LDR-L1 (OURS)	-505.066 ± 0.001	26.10 ± 0.12	(2.84 ± 0.12) $\times 10^{-3}$	(3.35 ± 0.03) $\times 10^{-3}$	(4.52 ± 0.13) $\times 10^{-3}$	(5.50 ± 0.06) $\times 10^{-3}$	(4.71 ± 0.87) $\times 10^{-2}$
ALANINE HEXAPEPTIDE	5×10^6	FWD KL	-505.174 ± 0.005	29.60 ± 0.25	(1.89 ± 0.04) $\times 10^{-3}$	(3.39 ± 0.01) $\times 10^{-3}$	(2.73 ± 0.12) $\times 10^{-3}$	(5.39 ± 0.07) $\times 10^{-3}$	(3.66 ± 0.63) $\times 10^{-2}$
		FWD KL + LDR-L2 (OURS)	-505.259 ± 0.010	38.70 ± 0.55	(3.30 ± 0.38) $\times 10^{-3}$	(2.44 ± 0.05) $\times 10^{-3}$	(5.64 ± 0.51) $\times 10^{-3}$	(4.26 ± 0.10) $\times 10^{-3}$	(4.18 ± 0.28) $\times 10^{-2}$
		FWD KL + LDR-L1 (OURS)	-505.308 ± 0.007	39.59 ± 0.44	(1.73 ± 0.05) $\times 10^{-3}$	(2.63 ± 0.05) $\times 10^{-3}$	(2.90 ± 0.09) $\times 10^{-3}$	(4.49 ± 0.10) $\times 10^{-3}$	(4.38 ± 0.73) $\times 10^{-2}$

Table 11. Results for training on biased datasets using importance sampling. We average over 4 independent experiments with standard deviations. For each number of IS samples, **bold** indicates methods whose performance is not statistically significantly different from the best-performing method (two-sided Welch's t-test with $p \geq 0.05$).

SYSTEM	# IS SAMPLES	METHOD	NLL ↓	ESS / % ↑	RAM KL ↓	RAM KL W. RW ↓	TICA KL ↓	TICA KL W. RW ↓	$\mathcal{E} \cdot \mathcal{W}_2$
ALANINE DIPEPTIDE	1×10^5	FWD KL	-214.114 ± 0.004	51.42 ± 0.42	(1.61 ± 0.07) $\times 10^{-2}$	(2.21 ± 0.29) $\times 10^{-3}$	(4.54 ± 0.34) $\times 10^{-3}$	(1.19 ± 0.11) $\times 10^{-3}$	(1.25 ± 0.40) $\times 10^{-2}$
		FWD KL + LDR-L2 ONLY ON IS (OURS)	-214.264 ± 0.001	69.04 ± 0.13	(7.17 ± 0.69) $\times 10^{-3}$	(1.49 ± 0.09) $\times 10^{-3}$	(2.79 ± 0.36) $\times 10^{-3}$	(7.71 ± 0.32) $\times 10^{-4}$	(7.53 ± 0.80) $\times 10^{-3}$
		FWD KL + LDR-L1 ONLY ON IS (OURS)	-214.251 ± 0.001	66.94 ± 0.24	(6.69 ± 0.15) $\times 10^{-3}$	(1.62 ± 0.11) $\times 10^{-3}$	(2.93 ± 0.28) $\times 10^{-3}$	(8.22 ± 0.60) $\times 10^{-4}$	(1.01 ± 0.30) $\times 10^{-2}$
		FWD KL + LDR-L2 ON BOTH (OURS)	-214.353 ± 0.001	83.20 ± 0.19	(2.57 ± 0.11) $\times 10^{-3}$	(1.29 ± 0.03) $\times 10^{-3}$	(1.22 ± 0.06) $\times 10^{-3}$	(6.77 ± 0.44) $\times 10^{-4}$	(5.76 ± 0.80) $\times 10^{-3}$
		FWD KL + LDR-L1 ON BOTH (OURS)	-214.345 ± 0.001	82.30 ± 0.13	(3.26 ± 0.19) $\times 10^{-3}$	(1.23 ± 0.03) $\times 10^{-3}$	(1.51 ± 0.19) $\times 10^{-3}$	(6.10 ± 0.13) $\times 10^{-4}$	(7.00 ± 1.94) $\times 10^{-3}$
ALANINE DIPEPTIDE	1×10^6	FWD KL	-214.287 ± 0.001	73.45 ± 0.15	(5.75 ± 0.32) $\times 10^{-3}$	(2.56 ± 0.24) $\times 10^{-3}$	(2.30 ± 0.26) $\times 10^{-3}$	(1.37 ± 0.20) $\times 10^{-3}$	(6.50 ± 1.46) $\times 10^{-3}$
		FWD KL + LDR-L2 ONLY ON IS (OURS)	-214.406 ± 0.000	92.69 ± 0.03	(1.88 ± 0.02) $\times 10^{-3}$	(1.36 ± 0.07) $\times 10^{-3}$	(1.10 ± 0.03) $\times 10^{-3}$	(7.37 ± 0.31) $\times 10^{-4}$	(6.26 ± 1.07) $\times 10^{-3}$
		FWD KL + LDR-L1 ONLY ON IS (OURS)	-214.406 ± 0.000	93.38 ± 0.03	(1.73 ± 0.02) $\times 10^{-3}$	(1.27 ± 0.04) $\times 10^{-3}$	(1.04 ± 0.03) $\times 10^{-3}$	(6.73 ± 0.28) $\times 10^{-4}$	(5.38 ± 0.66) $\times 10^{-3}$
		FWD KL + LDR-L2 ON BOTH (OURS)	-214.416 ± 0.000	94.91 ± 0.05	(1.61 ± 0.04) $\times 10^{-3}$	(1.31 ± 0.05) $\times 10^{-3}$	(8.48 ± 0.71) $\times 10^{-4}$	(6.86 ± 0.65) $\times 10^{-4}$	(5.49 ± 1.24) $\times 10^{-3}$
ALANINE DIPEPTIDE	1×10^7	FWD KL	-214.383 ± 0.000	88.85 ± 0.03	(1.91 ± 0.05) $\times 10^{-3}$	(1.64 ± 0.04) $\times 10^{-3}$	(8.97 ± 0.36) $\times 10^{-4}$	(8.91 ± 0.27) $\times 10^{-4}$	(6.08 ± 1.49) $\times 10^{-3}$
		FWD KL + LDR-L2 ONLY ON IS (OURS)	-214.436 ± 0.000	98.78 ± 0.01	(1.37 ± 0.05) $\times 10^{-3}$	(1.30 ± 0.04) $\times 10^{-3}$	(8.24 ± 0.49) $\times 10^{-4}$	(7.17 ± 0.48) $\times 10^{-4}$	(5.29 ± 1.19) $\times 10^{-3}$
		FWD KL + LDR-L1 ONLY ON IS (OURS)	-214.434 ± 0.000	98.44 ± 0.01	(1.37 ± 0.05) $\times 10^{-3}$	(1.25 ± 0.05) $\times 10^{-3}$	(8.07 ± 0.32) $\times 10^{-4}$	(6.73 ± 0.39) $\times 10^{-4}$	(5.63 ± 1.53) $\times 10^{-3}$
		FWD KL + LDR-L2 ON BOTH (OURS)	-214.434 ± 0.000	98.48 ± 0.02	(1.41 ± 0.05) $\times 10^{-3}$	(1.34 ± 0.05) $\times 10^{-3}$	(8.26 ± 0.52) $\times 10^{-4}$	(6.99 ± 0.20) $\times 10^{-4}$	(6.31 ± 2.38) $\times 10^{-3}$
ALANINE DIPEPTIDE	1×10^7	FWD KL + LDR-L1 ONLY ON IS (OURS)	-214.431 ± 0.000	97.97 ± 0.03	(1.45 ± 0.04) $\times 10^{-3}$	(1.31 ± 0.04) $\times 10^{-3}$	(8.11 ± 0.22) $\times 10^{-4}$	(6.73 ± 0.21) $\times 10^{-4}$	(6.64 ± 1.43) $\times 10^{-3}$

Table 12. Results for variational training without data from the target distribution. We average over 4 independent experiments with standard deviations for alanine dipeptide and 3 independent experiments for alanine hexapeptide. For each number of target evaluations, **bold** indicates methods whose performance is not statistically significantly different from the best-performing method (two-sided Welch’s t-test with $p \geq 0.05$).

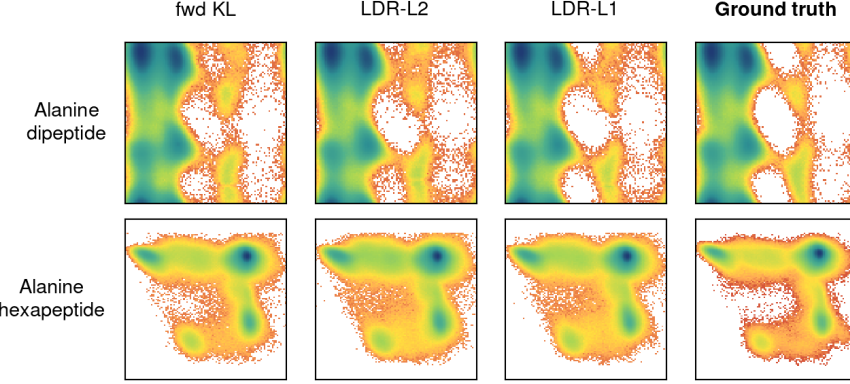
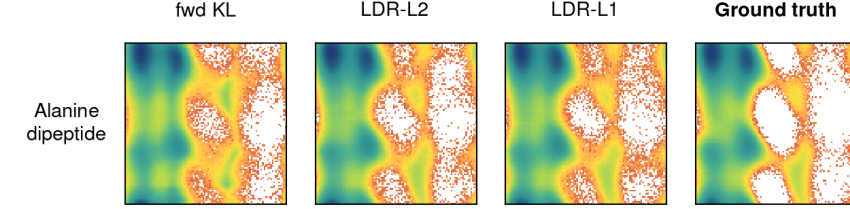
SYSTEM	# TARGET EVALS	METHOD	NLL ↓	ESS / % ↑	RAM KL ↓	RAM KL W. RW ↓	TICA KL ↓	TICA KL W. RW ↓	$\mathcal{E} \cdot \mathcal{W}_2$
ALANINE DIPEPTIDE	2.13×10^8	FAB	-214.412 ± 0.001	94.95 ± 0.12	$(1.51 \pm 0.04) \times 10^{-3}$	$(1.22 \pm 0.03) \times 10^{-3}$	$(3.05 \pm 0.40) \times 10^{-3}$	$(6.30 \pm 0.12) \times 10^{-4}$	$(5.89 \pm 0.77) \times 10^{-3}$
		TA-BG	-214.419 ± 0.002	95.76 ± 0.25	$(1.91 \pm 0.13) \times 10^{-3}$	$(1.34 \pm 0.06) \times 10^{-3}$	$(2.72 \pm 0.80) \times 10^{-3}$	$(1.08 \pm 0.17) \times 10^{-3}$	$(8.70 \pm 1.71) \times 10^{-3}$
		CMT	-214.358 ± 0.003	85.20 ± 0.47	$(3.78 \pm 0.38) \times 10^{-3}$	$(2.33 \pm 0.23) \times 10^{-3}$	$(2.16 \pm 0.71) \times 10^{-3}$	$(1.17 \pm 0.12) \times 10^{-3}$	$(5.36 \pm 1.20) \times 10^{-3}$
	1×10^7	CMT + LDR-L2 (OURS)	-214.429 ± 0.001	97.81 ± 0.08	$(1.62 \pm 0.05) \times 10^{-3}$	$(1.41 \pm 0.04) \times 10^{-3}$	$(9.36 \pm 0.07) \times 10^{-4}$	$(7.43 \pm 0.40) \times 10^{-4}$	$(5.66 \pm 0.26) \times 10^{-3}$
		CMT + LDR-L1 (OURS)	-214.429 ± 0.001	97.84 ± 0.05	$(1.57 \pm 0.09) \times 10^{-3}$	$(1.42 \pm 0.08) \times 10^{-3}$	$(9.47 \pm 0.44) \times 10^{-4}$	$(7.46 \pm 0.70) \times 10^{-4}$	$(5.70 \pm 0.65) \times 10^{-3}$
		CMT	-214.405 ± 0.001	93.18 ± 0.19	$(1.70 \pm 0.03) \times 10^{-3}$	$(1.52 \pm 0.03) \times 10^{-3}$	$(1.40 \pm 0.33) \times 10^{-3}$	$(7.94 \pm 0.68) \times 10^{-4}$	$(4.84 \pm 0.90) \times 10^{-3}$
	2×10^7	CMT + LDR-L2 (OURS)	-214.432 ± 0.000	98.41 ± 0.03	$(1.38 \pm 0.03) \times 10^{-3}$	$(1.29 \pm 0.06) \times 10^{-3}$	$(1.95 \pm 0.10) \times 10^{-3}$	$(9.73 \pm 0.55) \times 10^{-4}$	$(6.08 \pm 1.21) \times 10^{-3}$
		CMT + LDR-L1 (OURS)	-214.435 ± 0.001	98.81 ± 0.09	$(1.47 \pm 0.10) \times 10^{-3}$	$(1.29 \pm 0.10) \times 10^{-3}$	$(1.56 \pm 0.47) \times 10^{-3}$	$(8.96 \pm 1.75) \times 10^{-4}$	$(8.37 \pm 1.48) \times 10^{-3}$
		CMT	-214.431 ± 0.000	97.85 ± 0.05	$(1.46 \pm 0.04) \times 10^{-3}$	$(1.39 \pm 0.03) \times 10^{-3}$	$(1.78 \pm 0.04) \times 10^{-3}$	$(1.09 \pm 0.04) \times 10^{-3}$	$(6.75 \pm 2.05) \times 10^{-3}$
	1×10^8	CMT + LDR-L2 (OURS)	-214.437 ± 0.001	99.11 ± 0.06	$(1.39 \pm 0.04) \times 10^{-3}$	$(1.36 \pm 0.03) \times 10^{-3}$	$(1.94 \pm 0.42) \times 10^{-3}$	$(1.11 \pm 0.08) \times 10^{-3}$	$(7.65 \pm 2.06) \times 10^{-3}$
		CMT + LDR-L1 (OURS)	-214.438 ± 0.000	99.29 ± 0.04	$(1.42 \pm 0.03) \times 10^{-3}$	$(1.32 \pm 0.02) \times 10^{-3}$	$(1.81 \pm 0.05) \times 10^{-3}$	$(1.12 \pm 0.07) \times 10^{-3}$	$(8.92 \pm 0.64) \times 10^{-3}$
		FAB	-504.355 ± 0.019	14.41 ± 0.27	$(2.15 \pm 0.12) \times 10^{-2}$	$(1.02 \pm 0.05) \times 10^{-2}$	$(3.62 \pm 0.06) \times 10^{-2}$	$(1.57 \pm 0.07) \times 10^{-2}$	$(3.38 \pm 1.25) \times 10^{-2}$
	4.2×10^8	TA-BG	-504.782 ± 0.019	18.66 ± 0.16	$(6.74 \pm 1.29) \times 10^{-3}$	$(6.74 \pm 0.89) \times 10^{-3}$	$(8.19 \pm 1.17) \times 10^{-3}$	$(1.14 \pm 0.10) \times 10^{-2}$	$(1.60 \pm 0.49) \times 10^{-2}$
		CMT	-503.190 ± 0.051	5.92 ± 0.37	$(6.72 \pm 0.73) \times 10^{-2}$	$(5.23 \pm 0.51) \times 10^{-2}$	$(1.56 \pm 0.45) \times 10^{-1}$	$(1.07 \pm 0.43) \times 10^{-1}$	$(8.30 \pm 1.78) \times 10^{-2}$
		CMT + LDR-L2 (OURS)	-504.801 ± 0.008	31.47 ± 0.71	$(1.61 \pm 0.08) \times 10^{-3}$	$(1.56 \pm 0.23) \times 10^{-2}$	$(1.33 \pm 0.06) \times 10^{-2}$	$(1.58 \pm 0.08) \times 10^{-2}$	$(5.92 \pm 1.28) \times 10^{-2}$
	4×10^8	CMT + LDR-L1 (OURS)	-504.721 ± 0.010	29.48 ± 0.40	$(1.71 \pm 0.03) \times 10^{-3}$	$(1.65 \pm 0.05) \times 10^{-2}$	$(1.30 \pm 0.15) \times 10^{-2}$	$(1.77 \pm 0.14) \times 10^{-2}$	$(6.35 \pm 0.33) \times 10^{-2}$
		CMT	-503.545 ± 0.364	20.85 ± 0.65	$(9.08 \pm 3.16) \times 10^{-2}$	$(8.32 \pm 3.59) \times 10^{-2}$	$(1.89 \pm 0.19) \times 10^{-1}$	$(1.41 \pm 0.24) \times 10^{-1}$	$(3.96 \pm 1.52) \times 10^{-2}$
		CMT + LDR-L2 (OURS)	-505.012 ± 0.004	41.71 ± 0.47	$(9.05 \pm 0.65) \times 10^{-3}$	$(1.02 \pm 0.03) \times 10^{-2}$	$(8.81 \pm 0.50) \times 10^{-3}$	$(1.12 \pm 0.01) \times 10^{-2}$	$(3.32 \pm 0.54) \times 10^{-2}$
	2×10^9	CMT + LDR-L1 (OURS)	-505.051 ± 0.013	43.66 ± 0.69	$(7.78 \pm 0.06) \times 10^{-3}$	$(8.30 \pm 0.28) \times 10^{-3}$	$(8.65 \pm 0.28) \times 10^{-3}$	$(1.07 \pm 0.04) \times 10^{-2}$	$(2.96 \pm 0.64) \times 10^{-2}$
		CMT	-504.770 ± 0.037	23.95 ± 0.34	$(1.39 \pm 0.07) \times 10^{-2}$	$(1.27 \pm 0.06) \times 10^{-2}$	$(1.54 \pm 0.08) \times 10^{-2}$	$(1.88 \pm 0.05) \times 10^{-2}$	$(6.17 \pm 0.55) \times 10^{-2}$
		CMT + LDR-L2 (OURS)	-505.193 ± 0.007	47.76 ± 0.31	$(5.08 \pm 0.12) \times 10^{-3}$	$(5.52 \pm 0.06) \times 10^{-3}$	$(6.53 \pm 0.07) \times 10^{-3}$	$(7.07 \pm 0.10) \times 10^{-3}$	$(1.22 \pm 0.19) \times 10^{-2}$
		CMT + LDR-L1 (OURS)	-505.219 ± 0.019	48.32 ± 0.66	$(5.06 \pm 0.94) \times 10^{-3}$	$(5.88 \pm 0.70) \times 10^{-3}$	$(6.25 \pm 0.58) \times 10^{-3}$	$(7.82 \pm 0.72) \times 10^{-3}$	$(1.48 \pm 0.29) \times 10^{-2}$

Table 13. Results for training on Cartesian coordinates using an unbiased dataset from the target distribution of alanine dipeptide. We average over 4 independent experiments with standard deviations. **Bold** indicates methods whose performance is not statistically significantly different from the best-performing method (two-sided Welch’s t-test with $p \geq 0.05$).

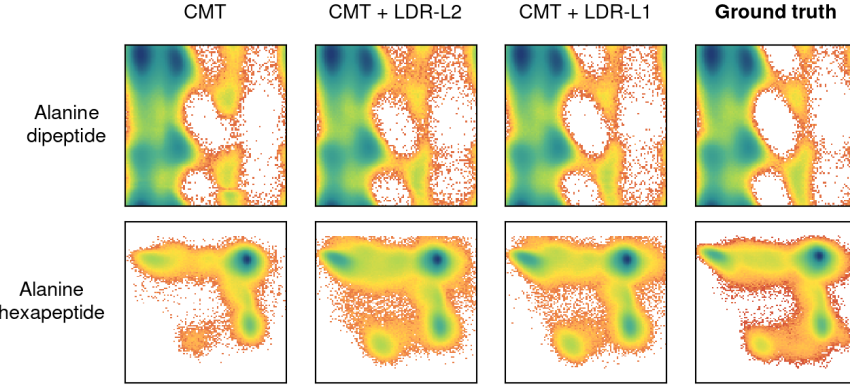
METHOD	NLL ↓	ESS / % ↑	RAM KL ↓	RAM KL W. RW ↓	$\mathcal{E} \cdot \mathcal{W}_2$
FWD KL (Tan et al., 2025a)	-219.583 ± 0.051	19.40 ± 0.80	$(2.93 \pm 0.29) \times 10^{-2}$	$(2.87 \pm 0.06) \times 10^{-2}$	$(1.51 \pm 0.20) \times 10^{-1}$
FWD KL*	-219.583 ± 0.050	27.32 ± 1.28	$(2.93 \pm 0.30) \times 10^{-2}$	$(2.51 \pm 0.08) \times 10^{-2}$	$(1.43 \pm 0.09) \times 10^{-1}$
FWD KL* (PATH)	-218.528 ± 0.090	10.31 ± 0.86	$(1.04 \pm 0.11) \times 10^{-1}$	$(4.77 \pm 0.95) \times 10^{-2}$	$(1.77 \pm 0.15) \times 10^{-1}$
FWD KL* + LDR-L2 (OURS)	-219.815 ± 0.034	35.89 ± 1.69	$(2.50 \pm 0.35) \times 10^{-2}$	$(1.79 \pm 0.10) \times 10^{-2}$	$(9.27 \pm 2.20) \times 10^{-2}$
FWD KL* + LDR-L1 (OURS)	-219.800 ± 0.044	35.75 ± 1.63	$(2.16 \pm 0.08) \times 10^{-2}$	$(2.07 \pm 0.23) \times 10^{-2}$	$(1.15 \pm 0.33) \times 10^{-1}$

* Uses our improved augmentation correction, see Appendix C.1.

F. Visualizations

(a) Training on unbiased datasets (1×10^6 samples)(b) Training on biased datasets (1×10^5 IS samples)

(c) Variational training with CMT



(d) Cartesian coordinates: Training on unbiased datasets

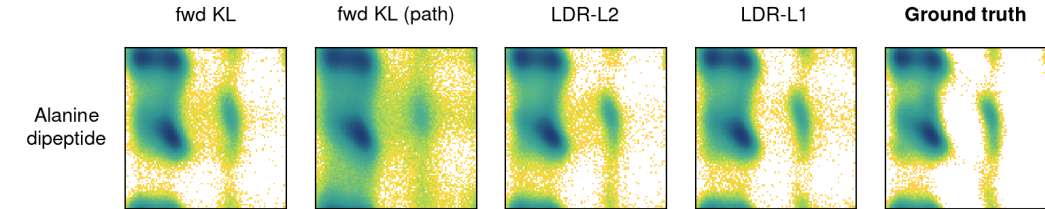


Figure 7. Visualization of the 2D marginals of the main degrees of freedom for each system. For alanine dipeptide, we show the marginal of the two main dihedral angles (Ramachandran), for alanine hexapeptide the 2D TICA projection. (a) Training on unbiased datasets using 1×10^6 samples, (b) training on biased dataset using 1×10^5 IS samples, (c) variational training with CMT (1×10^7 target evaluations for alanine dipeptide, 1×10^8 for alanine hexapeptide), (d) training in Cartesian coordinates on unbiased dataset (1×10^5 samples).